

POLITECNICO DI TORINO

Master of Science
in Mathematical Engineering

Master's Degree Thesis

**On Phase-Field Modeling of Fracture
in a Computational Framework**



Supervisor

prof. Alberto Giuseppe Sapora

Co-supervisor

dr. Amir Mohammed Mirzaei

Candidate

Giacomo Petraglia

Academic Year 2022-2023

March 24, 2023

A mamma, papà e Enrica

Summary

Phase-Field represents one of the most versatile numerical method to describe a large variety of physical phenomena related to Continuum and Fracture Mechanics. Instead of using strict boundary conditions at the interface, this method employs a partial differential equation to describe the behavior of an auxiliary field (known as the phase field) that acts as an order parameter. In this dissertation, the phase-field model is applied to investigate crack initiation and growth in brittle notched structures under mode I loading conditions and numerical outcomes are compared with experimental results available in the literature. Firstly, a one-dimensional (1D) benchmark is defined giving particular attention to modelling definitions (e.g. how degradation functions depend on damage rise and growth) and stability concepts, investigating under which conditions damage localizes. An original MATLAB® code is developed, whose logic and structure are broadly analyzed. Numerical results are then provided for 2D case, by considering the effect of circular holes and re-entrant corners on structural strength. From a computational point of view, we exploit Abaqus/FORTRAN coupling potentialities through UEL (User defined ELe ment) subroutines implementation. This work opens up to extend simulation results on damage trajectories predictions, in order to furnish to the analyzed structures also a morphological fracture characterization.

Contents

List of Tables	7
List of Figures	9
1 Phase-Field fracture modelling: application to 1D problems	13
1.1 Theoretical aspects	14
1.1.1 Introduction: model emergence	14
1.1.2 A possible model formulation	15
1.1.3 Variational approach	16
1.2 Model application example: 1D tensile test	17
1.2.1 Damage law definition	17
1.2.2 Analytical solution	19
1.2.3 Homogeneous solutions stability	20
1.3 Algorithm structure and numerical discretization	22
1.3.1 \mathcal{P} minimization form with respect to u	22
1.3.2 \mathcal{P} minimization form with respect to α	24
1.4 MATLAB® code analysis	25
1.4.1 <code>main</code> and <code>DiffusionAssembler</code> function	25
1.4.2 <code>minalpha</code> function	26
1.5 Simulation results	28
1.5.1 Damage field $\alpha(x, t)$	28
1.5.2 Stress σ_t	29
1.5.3 Elastic energy E_{el}	30
1.5.4 Dissipated energy E_{diss}	30
2 Phase-Field fracture modelling: theoretical and computational features for 2D domains	33
2.1 Theoretical notes	33
2.1.1 Fracture smooth topology: a quadratic local energy term justification	34
2.1.2 AT1 and AT2 fracture modelling	36
2.2 Numerical formulation	37
2.2.1 Balance laws weak form	37
2.2.2 Balance laws discrete form	38
2.3 Analysis definition on software	40

2.3.1	Plane strain conditions and geometry	41
2.3.2	Material properties	42
2.3.3	Boundary conditions	43
2.3.4	Mesh generation	43
2.4	FORTRAN subroutine structure	47
3	2D simulations results	53
3.1	Circular Holes: size effect	53
3.1.1	Materials properties definition	54
3.1.2	PMMA results	55
3.1.3	GPPS results	57
3.2	Strength decrease due to sharp V-notches	58
3.2.1	a = 1 cm	59
3.2.2	a = 2 cm	60
4	Conclusions and future perspectives	63

List of Tables

2.1	Specimens generic dimensions. These values refer to the entire physical geometry: the measures entered in the Abaqus model definition vary according to the specific geometry symmetry properties. R is the <i>hole radius</i> for the size effect analysis; a represents the <i>notch depth</i> for V-notch effect analysis.	42
2.2	Correspondences between Listing 2.4 code lines with residuals and stiffness matrix expressions.	51
3.1	Measured experimental material properties: Young's modulus E , Poisson's ratio ν , ultimate tensile strength σ_M and fracture toughness K_{IC} . For PMMA properties are taken from Ayatollahi and Torabi (2010), whereas for GPPS from Torabi et al. (2016).	55
3.2	Derived material properties: critical energy release rate G_c , physical characteristic length ℓ_{ch} , numerical characteristic length ℓ_2 and minimum mesh element size h_{min}	55
3.3	PMMA failure stress σ_{cr} experimental results and respective numerical outcomes. Simulations mildly overestimate real failure stress values for all the considered radii.	57
3.4	GPPS failure stress σ_{cr} experimental results and respective numerical outcomes. Simulations mildly overestimate real failure stress values for $R = 0.5, 1, 2$ mm. Critical stress estimations underestimate experimental data for $R = 0$ mm (no hole case, σ_M prediction) and $R = 0.25$ mm.	57
3.5	Failure load P_{cr} experimental results and respective numerical outcomes for $\mathbf{a} = \mathbf{1}$ cm. Simulation data do not match the respective experimental values.	60
3.6	Failure load P_{cr} experimental results and respective numerical outcomes for $\mathbf{a} = \mathbf{1}$ cm. Differently from Table 3.5, values are normalized with respect to $P_{180^\circ} = P_{cr}(\beta = 180^\circ)$. Normalized experimental and numerical datasets match correctly.	61
3.7	Failure load P_{cr} experimental results and respective numerical outcomes for $\mathbf{a} = \mathbf{2}$ cm. Although simulation data do not match the respective experimental values, a moderate level of agreement is observed.	62

3.8 Failure load P_{cr} experimental results and respective numerical outcomes for $\mathbf{a} = \mathbf{2\ cm}$. Differently from Table 3.7, values are normalized with respect to $P_{180^\circ} = P_{cr}(\beta = 180^\circ)$. Normalized experimental and numerical datasets are in quite perfect alignment. 62

List of Figures

1.1	A 1D tensile test representation: the specimen is clamped at $x = 0$ and subjected to an imposed displacement $u_t(x = L) = U_t$ (i.e. a Dirichlet boundary condition) at $x = L$	17
1.2	Damage field $\alpha(x, t)$ plot. Simulation data capture the main difference between the two cases: the <i>transition smoothness</i> between the elastic and the damage phase, as explained in Sect. 1.2.2 and 1.2.3.	29
1.3	Maximum $\alpha_t(x)$ plot over t . The <i>transition smoothness</i> difference is caught also in this graphs.	29
1.4	Uniform stress σ_t plot. In both cases there is a sharp trend change for $t > t^*$. For the long bar case, the stress drops to zero due to the immediate damage instability emergence. For the short bar case, for $t^* < t < t_{cr}$, the stress follows the theoretical trend reported in (1.23c) (i.e. the stable damaging phase).	30
1.5	Elastic energy E_{el} plot. During elastic phase, the material absorbs energy in a quadratic manner. For $t > 1$, the elastic energy decrease differs according to the stable damaging phase presence.	31
1.6	Fracture dissipated energy E_{diss} plot. For $t < 1$, during the elastic phase, the energy is null because the material is still unbroken. For $t > 1$, the energy growth trend changes depending on the fracture process stability status.	32
2.1	Two topology strategies to model 1D fracture.	35
2.2	CPE4 finite element structure, based on lagrangian basic functions.	39
2.3	Two geometries examples: hole geometry (see 2.3a) and Three Point Bending (TPB) geometry (see 2.3b).	41
2.4	Boundary conditions for a holed geometry. A YSYMM condition on the lower contour and an XSYMM condition on the left side are imposed. The applied displacement over the top contour is also displayed.	44
2.5	Typical boundary condition setup on TPB samples. A XSYMM condition over the right side and a $u_y = 0$ condition on the lower contour leftmost point (circled in red) are imposed. The applied concentrated force over the top contour (circled in green) is also displayed.	44

2.6	Mesh generated for a size effect analysis ($R = 2$ mm) and its detailed visualization. The element minimum size ($h_{\min} = \ell_2/5$) is fixed all along the bottom side. At a distance equal to 5 mm the element fixed size is $h_{\text{part}} = \ell_2$	45
2.7	Mesh generated for a TPB analysis ($a = 2$ mm, $\beta = 90^\circ$) and its detailed visualization. The element minimum size ($h_{\min} = \ell_2/5$) is fixed along the right contour lower half: this refined zone does not reach the geometry top side for a significant critical load underestimation. All over the circumference arc (visible also in 2.5) the element fixed size is $h_{\text{part}} = \ell_2$	46
3.1	Infinite tensile plate containing a circular hole. Maximum circumferential stress $\sigma_{\theta, \max} = 3\sigma$ is highlighted.	54
3.2	PMMA failure stress σ_{cr} experimental results and the respective numerical outcomes depending on hole radius R . The graphical comparison reveals a good matching between the two datasets.	56
3.3	GPPS failure stress σ_{cr} experimental results and the respective numerical outcomes depending on hole radius R	58
3.4	Normalized failure stress σ_{cr} numerical results (both PMMA and GPPS datasets), corresponding experimental values (from Sapora et al. (2018)) and the resistance decrease trend predicted by Finite Fracture Mechanics (from Sapora and Cornetti (2018)). Despite their different slopes, the numerical and theoretical decrease predictions tends both to the expected value (i.e. σ_{cr} decreases from σ_M ($R = 0$) to $\sigma_M/3$ for sufficiently large R , but still small with respect to the plate size).	59
3.5	Failure load P_{cr} numerical and experimental results depending on notch angle β for a = 1 cm . Datasets are normalized with respect to the unnotched case critical value (i.e. $P_{180^\circ} = P_{cr}(\beta = 180^\circ)$). The graphical comparison reveals a quite perfect matching between the two datasets.	60
3.6	Failure load P_{cr} numerical and experimental results depending on notch angle β for a = 2 cm . Datasets are normalized with respect to the unnotched case critical value (i.e. $P_{180^\circ} = P_{cr}(\beta = 180^\circ)$).The graphical comparison reveals a near-perfect alignment between the two datasets.	61

Listings

- 1.1 `main` function: for loop over time discretization 25
- 1.2 `DiffusionAssembler` function structure 26
- 1.3 `minalpha` function structure 27
- 2.1 Phase-Field UEL subroutine *incipit* 47
- 2.2 do cycle over current element nodes - Ist part 48
- 2.3 do cycle over current element nodes - IInd part 49
- 2.4 do cycle over current element nodes - IIIrd part 51

*That feeling in the air
Something was definitely there
It was a time when things were good
I felt peace in the neighborhood*

[P. MCCARTNEY,
Peace in the Neighborhood
Off the Ground, 1993]



Chapter 1

Phase-Field fracture modelling: application to 1D problems

Fracture Mechanics is the mechanical analysis of materials containing cracks, notches or holes. Acting as stress raisers, they can reduce significantly the strength of the structural component under investigation. Since the beginning of the last century, several leading researchers have investigated how the defect shape affects the structural resistance.

[Kirsch \(1898\)](#) pioneering work illustrates how a single circular hole in an infinite plate subjected to far field loading conditions leads to a *stress concentration* around the hole's edge. Subsequent works focus on structural resistance decrease for various hole geometries (see [Inglis \(1913\)](#) and [Westergaard \(1939\)](#) for sharp and elliptic cracks) but the proposed *tensile criterion* fails for limit cases, not capturing *in toto* materials' behavior.

[Griffith \(1921\)](#) provided an innovative approach based on *energy* considerations: the criterion allows to study damage emergence and its influence on structural strength without dealing with stresses discontinuities. Defining a fracture related energy contribution for a damaging mechanical system also permits to apply the robust and well-known *variational methods* to our modelling benchmark, as firstly shown in [Francfort and Marigo \(1998\)](#).

Phase-Field model emerges in computational modelling panorama as one of the most versatile method to numerically examine several physical phenomena, such as fluid dynamics in porous media (see [Shuwei et al. \(2019\)](#)) and morphological evolution of metallic materials under environmental attack (see [Ansari et al. \(2021\)](#)).

This first chapter will provide an overview of phase-field models applied to brittle fracture framework, by first discussing theoretical contexts, then analyzing an original MATLAB® code resolving damage problem for 1D domains and, finally, showing the simulation results.

1.1 Theoretical aspects

1.1.1 Introduction: model emergence

The phase-field approach applied to brittle fracture mechanics has its origin in the cutting-edge work by Griffith (1921), where for the first time crack initiation phenomena were investigated introducing energetic considerations. The criterion affirms that the crack propagates if the available energy release rate G (whose expression changes according to the experimental setup) exceeds a threshold value G_c (defined as *critical energy release rate*, or fracture energy).

This revolutionary study permitted to shift the focus on a modelling approach based on energetic assumptions. Francfort and Marigo (1998) firstly proposed to define an energy functional dependent on the displacement \mathbf{u} and the crack surface Γ :

$$W(\mathbf{u}, \Gamma) = \psi^{\text{el}}(\mathbf{u}, \Gamma) + \psi^{\text{fr}}(\Gamma), \quad (1.1)$$

where the first addendum refers to the elastic energy term and the second one refers to the Griffith-like crack energy release (details about the involved functional spaces will be provided in the next sections).

Let $\Omega \subset \mathbb{R}^n$ be a spatial region occupied by a linear elastic brittle material (with a stiffness tensor \mathbb{A} and a threshold energy release rate G_c). Finding the two unknown (\mathbf{u} and Γ) expressions consists on the resolution of the following variational problem:

$$\begin{aligned} (\mathbf{u}, \Gamma) = \operatorname{argmin} \mathcal{E}(\mathbf{u}, \Gamma) &= \int_{\Omega \setminus \Gamma} \frac{1}{2} [\mathbb{A} \varepsilon(\mathbf{u}) \cdot \varepsilon(\mathbf{u})] \, d\mathbf{x} + G_c \mathcal{H}^{n-1}(\Gamma), \\ \mathbf{u} = \mathbf{u}_t \quad \forall \mathbf{x} \in \partial_u \Omega := \Omega_u, \quad \sigma = \sigma_t \quad \forall \mathbf{x} \in \partial_F \Omega := \Omega_F, \end{aligned} \quad (1.2)$$

where $\varepsilon(\mathbf{u})$ is the *strain*, σ is the *stress* and $\mathcal{H}^{n-1}(\Gamma)$ is the *Hausdorff crack measure* in \mathbb{R}^{n-1} .

The Γ -convergence notion enables to fully resolve the variational problem in both variables and to lay a robust numerical groundwork, approximating the functional $\mathcal{E}(\mathbf{u}, \Gamma)$ with:

$$\mathcal{E}_\ell(\mathbf{u}, \alpha, \nabla \alpha) = \int_{\Omega} \frac{1}{2} [\mathbb{A}(\alpha) \varepsilon(\mathbf{u}) \cdot \varepsilon(\mathbf{u})] \, d\mathbf{x} + \frac{G_c}{4c_w} \int_{\Omega} \frac{w(\alpha)}{\ell} + C\ell |\nabla \alpha|^2 \, d\mathbf{x}, \quad (1.3)$$

where $\alpha \in [0, 1]$ represents the “phase-field” damage variable, C and $c_w := \int_0^1 \sqrt{w(\alpha)} d\alpha$ are normalization constants and $\ell > 0$ is a length regularization parameter. The functions $\mathbb{A}(\alpha)$ and $w(\alpha)$ are the defining model equations, describing the stiffness degradation with increasing damage and the energy dissipation caused by damage propagation, respectively. All these mathematical parameters will be deeply discussed in the following sections.

The \mathcal{E}_ℓ expression lends itself well to be formulated in its finite element discretization and the Γ -convergence notion guarantees that if \mathcal{E}_ℓ Γ -converges to \mathcal{E} then the functions (\mathbf{u}, Γ) that globally minimize \mathcal{E}_ℓ converge to the global minimizers of \mathcal{E} ¹.

¹This assumption is valid under some conditions on the abovementioned parameters and functions, that will be always guaranteed for all the model (1.3) variations focused in this work. For further information about Γ -convergence notion, see Braides (2002).

Two specific models based on (1.3) will be developed in the following: the first one applied to a 1D framework (Chapter 1); the second one applied to a 2D environment (Chapter 2). It should be clarified that the differences between the proposed models do not depend on the geometrical dimensions of the domain and they can be switched without any compatibility issues.

1.1.2 A possible model formulation

Let $(\mathbf{x}, t) \in \Omega \times I$, $\Omega \subset \mathbb{R}^n$, $I = [0, t^*]$, $t^* \in \mathbb{R}^+$ be the spatio-temporal domain of the problem. As shown in Pham et al. (2011) and basing on Sect. 1.1.1 concepts, it is fundamental to start by the definition of the approximated state function W_ℓ , characterizing the *energy density* $\forall x \in \Omega$. The modelling assumption is:

$$\begin{aligned} W_\ell(\varepsilon(\mathbf{u}), \alpha, \nabla\alpha) \circ (x) &= \left[\psi^{\text{el}}(\varepsilon(\mathbf{u}), \alpha) + \psi_\ell^{\text{fr}}(\alpha, \nabla\alpha) \right] \circ (x) = \\ &:= \underbrace{\frac{1}{2} [\mathbb{A}(\alpha) \varepsilon(\mathbf{u}) \cdot \varepsilon(\mathbf{u})] \circ (x)}_{\text{I}^{\text{st}} \text{ term}} + \underbrace{w(1) w(\alpha(x))}_{\text{II}^{\text{nd}} \text{ term}} + \underbrace{C w(1) \ell^2 \nabla\alpha(x) \cdot \nabla\alpha(x)}_{\text{III}^{\text{rd}} \text{ term}} \end{aligned} \quad (1.4)$$

In this energy density formulation several functions and variables come into play:

- $\varepsilon(\mathbf{u}(x)) = \frac{1}{2} [\nabla\mathbf{u} + (\nabla\mathbf{u})^T]$ represents the *local linearized strain*, whereas $\mathbf{u}(x)$ is the *displacement* vector.
- $\alpha(x)$ denotes the **damage variable**: it consists of a real and *continuous* function $\alpha = \alpha(x) \in [0,1]$ that evaluates the damaging state of the considered continuum $\forall x \in \Omega$. For our convention, when $\alpha(x = x_{\text{und}}) = 0$ the solid is undamaged and when $\alpha(x = x_{\text{dam}}) = 1$ the solid is fully damaged. It is interesting to note that $\alpha(x)$ represents a *phase-field* function describing the local damaging state.
- The variable $\alpha \mapsto \mathbb{A}(\alpha)$ is the *stiffness tensor*, that embraces the continuum elastic properties. Our modelling assumption implies that the material mechanical behavior is directly influenced by the local damaging state.
- The expression $\alpha \mapsto w(1) w(\alpha)$ stands for the *density of the dissipated energy* during a homogeneous damage process, where the damage variable grows from 0 to α in a quasi-static manner.
- The parameter ℓ , introduced into (1.4) in first instance for regularization reasons, represents the *characteristic length* of the material that controls the width of the damage localization zones.

The proposed expression (1.4) for the state function W_ℓ is made up of three contributions, each of which with a clear physical meaning:

Ist term: this is the classic *elastic energy* term in its generic formulation, where \mathbb{A} is a 4th rank tensor.

IInd term: this contribution evaluates the dissipated energy due to the damaging process in a point-wise manner; it can be interpreted as the *local* part of the fracture loss of energy.

IIIrd term: this is the *non-local* part of the dissipating energy that takes account into the fracture process in a neighborhood of $x \in \Omega$. This contribution plays a *stabilizing* role in the model, limiting the onset of strongly localized damaging sites, as clearly shown by Marigo and Pham (2009).

1.1.3 Variational approach

Let us define \mathbf{u}_t as the imposed displacement on the boundary portion $\partial\Omega_u$ (i.e. Dirichlet conditions), \mathbf{F}_t as the surface forces acting on the boundary portion $\partial\Omega_F$ (i.e. Neumann conditions) and \mathbf{f}_t as the resultant of the volume forces on Ω .

The spaces of the admissible displacement and damage fields are defined, respectively, as follows:

$$\mathcal{C}(U_t) = \left\{ \mathbf{v} \in [H^1(\Omega)]^n : \mathbf{v} = \mathbf{u}_t \text{ for } \partial\Omega_u \right\} \quad (1.5a)$$

$$\mathcal{D}_1 = \left\{ \beta \in H^1(\Omega) : \beta(x) \in [0,1] \text{ a.e. in } \Omega \right\} \quad (1.5b)$$

At this point it is possible to express the *energy functional* for the quasi-static evolution problem:

$$\begin{aligned} \mathcal{P}_t(\mathbf{u}, \alpha) \circ (x) &:= \int_{\Omega} W_{\ell}(\varepsilon(\mathbf{u}), \alpha, \nabla\alpha) \circ (x) \, d\Omega - \int_{\partial\Omega_F} \mathbf{F}_t \cdot \mathbf{u}(x) \, d\Gamma - \int_{\Omega} \mathbf{f}_t \cdot \mathbf{u}(x) \, d\Omega, \\ (\mathbf{u}, \alpha) &\in \mathcal{C}(U_t) \times \mathcal{D}_1 \end{aligned} \quad (1.6)$$

Specifically for this case, the variational problem takes the form:

$$\begin{aligned} &\text{Find } (\mathbf{u}_t, \alpha_t) \in \mathcal{C}(\mathbf{u}_t) \times \mathcal{D}_1 \text{ such that:} \\ &\mathfrak{D}\mathcal{P}(\mathbf{u}_t, \alpha_t)(\mathbf{v} - \dot{\mathbf{u}}_t, \beta - \dot{\alpha}_t) \geq 0, \quad \forall (\mathbf{v}, \beta) \in \mathcal{C}(\dot{U}_t) \times \mathcal{D} \\ &\text{and } (\dot{\mathbf{u}}_t, \dot{\alpha}_t) \in \mathcal{C}(\dot{\mathbf{u}}_t) \times \mathcal{D}, \end{aligned} \quad (1.7)$$

where the dot represents the time derivative. The problem has to be solved $\forall t \in I$ and with the initial condition $\alpha_{t=0}(x) = 0$ (i.e. the body is initially undamaged). The functional space \mathcal{D} includes all the positive damage rates:

$$\mathcal{D} = \left\{ \beta \in H^1(\Omega) : \beta(x) \geq 0 \text{ a.e. in } \Omega \right\} \quad (1.8)$$

The differential operator \mathfrak{D} denotes the *functional* (or *Gateaux*) derivative, that evaluates the functional variation with respect to the functions on which the functional depends.

It is worthy to note that the fracture quasi-static evolution problem defined above can be seen as a *first-order unilateral minimality* condition on the energy functional defined in (1.6): *first-order* because of the considered Gateaux derivative order; *unilateral* because of the **irreversibility condition** on the damage variable (the material cannot self-heals, mathematically $\dot{\alpha} \geq 0, \forall t$); *minimality* because the variational approach consists of finding the displacement and damage fields that, for a fixed time, minimize the energy functional. This explanation clearly justifies also the functional derivative application.

1.2 Model application example: 1D tensile test

In this section the mathematical model defined by the variational problem (1.7) is applied to a one-dimensional tensile test involving a clamped homogeneous bar of length L , with an imposed and time-dependent displacement to the free-end, as shown in Fig. 1.1.



Figure 1.1: A 1D tensile test representation: the specimen is clamped at $x = 0$ and subjected to an imposed displacement $u_t(x = L) = U_t$ (i.e. a Dirichlet boundary condition) at $x = L$.

For this classical example, the boundary and initial conditions are reported in the following, adopting a linear end-displacement with respect to the time:

$$u_t(x = 0) = 0, \quad \forall t \in I, \quad u_t(x = L) = U_t = L \cdot t, \quad t \in I \quad (1.9a)$$

$$\alpha_{t=0}(x) = 0, \quad \forall x \in \Omega, \quad \Omega = [0, L] \quad (1.9b)$$

Hence, the energy functional (1.6) takes the form:

$$\mathcal{P}(u, \alpha) = \int_0^L \left[\frac{1}{2} E(\alpha) \left(\frac{\partial u}{\partial x} \right)^2 + w(1) w(\alpha) + \frac{1}{2} w(1) \ell^2 \left(\frac{\partial \alpha}{\partial x} \right)^2 \right] dx, \quad (1.10)$$

where the x and t dependencies are omitted for the sake of brevity. Observing the elasticity energy part (i.e. the 1st term) a *scalar* elastic modulus $E(\alpha)$ takes over from the stiffness tensor, because of the one-dimensional domain.

1.2.1 Damage law definition

To describe the material specific features, the following damage law is introduced:

$$E(\alpha) = E_0 (1 - \alpha)^2, \quad w(\alpha) = \alpha \quad \left(E_0 = 29 \text{ GPa}, \quad w_1 = w(1) = 698 \text{ N/m}^2 \right) \quad (1.11)$$

The parameters E_0 (the elastic modulus for the undamaged material) and w_1 (a damage dissipation rate) were evaluated empirically for concrete, as reported in [Comi and Perego](#)

(2001). To guarantee this model consistency with (1.3):

$$\begin{cases} c_w = \int_0^1 \sqrt{w(\alpha)} \, d\alpha = \int_0^1 \sqrt{\alpha} \, d\alpha = \frac{2}{3} \\ w_1 = \frac{G_c}{4c_w \ell} \end{cases} \implies w_1 = \frac{3G_c}{8\ell}, \quad G_c = \frac{8}{3}\ell w_1 \quad (1.12)$$

The law (1.11) fulfills the *constitutive relations*:

- the functions $\alpha \mapsto E(\alpha), w(\alpha)$ are continuously differentiable on Ω ;
- the material has a positive stiffness for incomplete damage: $E(\alpha) > 0, \alpha \in [0,1)$;
- the material has no rigidity for complete damage: $E(\alpha = 1) = 0$;
- the stiffness decreases for increasing damage rate: $\frac{\partial E}{\partial \alpha} < 0$;
- the dissipation energy:
 - is positive during fracture processes: $w(\alpha) > 0, \alpha \in (0,1]$;
 - is null for intact materials: $w(\alpha = 0) = 0$;
 - does not decrease for growing damage states: $\frac{\partial w}{\partial \alpha} \geq 0$.

The choice of the damage law changes the admissible strains and stresses during the crack initiation and evolution. In fact, the law (1.11) refers to a *strain hardening* and *stress softening* material:

Strain hardening: the damage law satisfies

$$\frac{\partial w}{\partial \alpha} \frac{\partial^2 E}{\partial \alpha^2} - \frac{\partial^2 w}{\partial \alpha^2} \frac{\partial E}{\partial \alpha} > 0 \quad (1.13)$$

i.e. the domain of admissible strains increases for increasing damage;

Stress softening: the damage law satisfies

$$\frac{\partial w}{\partial \alpha} \frac{\partial^2 S}{\partial \alpha^2} - \frac{\partial^2 w}{\partial \alpha^2} \frac{\partial S}{\partial \alpha} > 0, \quad (1.14)$$

i.e. the domain of admissible stresses decreases for increasing damage. The function $S(\alpha) = E^{-1}(\alpha)$ is the *mechanical compliance*.

The damage law properties (1.13) and (1.14) are fundamental to study the *homogeneous solution stability*, as reported in the next sections.

1.2.2 Analytical solution

The stress $\sigma_t(x)$ equilibrium equation and the damage state equation (i.e. the strong form of the variational problem) can be obtained testing the inequality defining (1.7) with proper function classes:

- Testing with $v \in \mathcal{C}(\dot{u}_t)$ and $\beta = \dot{\alpha}_t$:

$$\frac{\partial \sigma_t}{\partial x}(x) = 0, \quad \sigma_t(x) = \left[E(\alpha_t) \frac{\partial u_t}{\partial x} \right] \circ (x), \quad \forall (x, t) \in ((0, L) \times I) \quad (1.15)$$

focusing on the *homogeneous solution* (tx, α_t) (for which the unknown fields result uniform throughout the spatial domain) and for the boundary conditions (1.9a), the displacement field satisfies:

$$\frac{\partial u_t}{\partial x}(x) = t, \quad u_t(x) = tx \quad \longrightarrow \quad \sigma_t(x) = tE(\alpha_t(x)) \quad (1.16)$$

- Testing with $v = \dot{u}_t$ and $\beta \in \mathcal{D}$ a strong formulation of the damage evolution problem in the form of *Kuhn-Tucker conditions*² can be obtained, involving among the other the following relations:

$$\mathfrak{R}_t(\alpha_t) := \frac{t^2}{2} \frac{\partial E}{\partial x}(\alpha_t) + \frac{\partial w}{\partial x}(\alpha_t) \geq 0 \quad (1.17a)$$

$$\dot{\alpha}_t \cdot \mathfrak{R}_t(\alpha_t) = 0 \quad (1.17b)$$

This means that since the *damage criterion* (1.17a) remains a strict inequality, the material remains intact (because of the *energy balance* (1.17b) $\longrightarrow \dot{\alpha}_t = 0$).

In this case, considering the damage law (1.11) and the initial condition (1.9b), a *damaging phase* following an *elastic phase* is clearly noticeable:

Elastic phase: Let define U_e as the displacement that nullifies the damage criterion:

$$\begin{cases} U_e = Lt^* \rightarrow t^* = \frac{U_e}{L} \\ t^{*2} E'(\alpha_{t=0} = 0) + 2w'(\alpha_{t=0} = 0) = 0 \end{cases} \Rightarrow U_e := -L \sqrt{\frac{2w'(0)}{E'(0)}} = L \sqrt{\frac{w_1}{E_0}}, \quad (1.18)$$

where $f' = \frac{\partial f}{\partial x}$ and t^* represents the *transition time* between the state stages. For $t \in I$ such that $U_t = Lt < U_e$, the damage criterion (1.17a) becomes a strict inequality. Owing to the *strain hardening* material characterization, the relation $\frac{w'}{E'}$ is a monotonic increasing function.

This considerations allow us to affirm that for $0 \leq t < t^*$ the damage rate is fixed to its initial value ($\alpha_{t=0} = 0$), because the energy balance (1.17b) remains valid. The time-strain interval $(0, t^*)$ defines the **elastic phase**, for which the system energy evolution does not involve any fracture phenomenon. According to (1.16), the stress grows linearly with respect to the temporal variable, in particular:

$$\sigma_t = tE(\alpha_{t=0} = 0) = tE_0 = \frac{U_t}{L} E_0, \quad \forall x \in \Omega \quad (1.19)$$

²This is a classical form to express the unilateral constrained minimization problems in their strong formulation. To investigate the method, see Gass and Fu (2013).

Damaging phase: For $U_t \geq U_e$ the damage criterion (1.17a) consists of an equality, hence $\dot{\alpha}_t$ can be a nonzero value. This means that the damage rate can increase (homogeneously under certain conditions that will be discussed in Sect. 1.2.3) satisfying the relation:

$$\frac{U_t}{L} = -\sqrt{\frac{2w'(\alpha_t)}{E'(\alpha_t)}} \longrightarrow \alpha_t = 1 - \left(\frac{U_e}{U_t}\right)^2 \quad (1.20)$$

Let define the *peak stress*:

$$\sigma_M := \sup_{\alpha \in [0,1]} \sqrt{\frac{2w'(\alpha)}{S'(\alpha)}} \quad (1.21)$$

Applying the damage law (1.11) it is trivial to show that³:

$$\sigma_M = \sigma_e := \sqrt{\frac{2w'(0)}{S'(0)}} \quad (1.22)$$

Using the peak stress expression, it is possible to express the complete analytical (and *homogeneous*) solution:

$$U_e = -L\sqrt{\frac{2w'(0)}{E'(0)}} = L\sqrt{\frac{w_1}{E_0}} = L\frac{\sigma_M}{E_0}, \quad (1.23a)$$

$$\sigma_e = \sigma_M = \sqrt{\frac{2w'(0)}{S'(0)}} = \sqrt{w_1 E_0}, \quad (1.23b)$$

$$\sigma_t = tE(\alpha_t) = \begin{cases} \frac{U_t}{L}E_0 = \sigma_M \frac{U_t}{U_e} & \text{for } U_t < U_e \text{ (elastic phase)} \\ \sigma_M \left(\frac{U_e}{U_t}\right)^3 & \text{for } U_t \geq U_e \text{ (damaging phase)} \end{cases} \quad (1.23c)$$

$$\alpha_t = \begin{cases} 0 & \text{for } U_t < U_e \text{ (elastic phase)} \\ 1 - \left(\frac{U_e}{U_t}\right)^2 & \text{for } U_t \geq U_e \text{ (damaging phase)} \end{cases} \quad (1.23d)$$

1.2.3 Homogeneous solutions stability

As investigated in Benallal and Marigo (2006), the proposed mathematical model includes some cases that allows unstable solutions, depending on the material assumed properties and geometrical parameters.

Intuitively, the stability study concerns the first directional derivative sign of the energy functional $\mathcal{P}_t(u, \alpha)$, with u and α admissible fields.

For $U_t < U_e$ (i.e. elastic phase) the homogeneous solution is always stable: being the damage criterion (1.17a) a strict inequality, the functional derivative fulfills $\mathfrak{D}\mathcal{P}_t(u, \alpha)(v, \beta) > 0$, $\forall (v, \beta) \in \mathcal{C}(0) \times \mathcal{D}$.

³It is provable that this assumption is valid in general for every stress softening damage law.

For $U_t \geq U_e$ (i.e. damaging phase) the damage criterion (1.17a) becomes an equality, implying that $\mathfrak{D}\mathcal{P}_t(u, \alpha)(v, \beta) = 0, \forall (v, \beta) \in \mathcal{C}(0) \times \mathcal{D}$. Hence to study the state stability it is necessary to evaluate the second functional derivative $\mathfrak{D}^2\mathcal{P}_t(u, \alpha)(v, \beta)$ (i.e. the first non-null Taylor expansion term of $\mathcal{P}_t(u, \alpha)$).

This analysis brings to the following assertion (as reported in Pham et al. (2011)):

Property 1.1 (Homogeneous solutions stability). *Let consider the physical benchmark referenced in Fig. 1.1.*

For $U_t < U_e$, the homogeneous state $(u_t, \alpha_t) = (tx, \alpha_{t=0} = 0)$ is always stable.

For $U_t \geq U_e$, the homogeneous state $(u_t, \alpha_t) = (tx, \alpha_t)$ (with α_t expression reported in (1.23d), damaging phase case):

- *is always stable if the damage law refers to a stress hardening material;*
- *is stable for stress softening material if and only if:*

$$\frac{L}{\ell} \leq \lambda_{cr} \frac{U_e}{U_t}, \quad \lambda_{cr} = \frac{4\pi}{3\sqrt{3}} \approx 2.4184 \quad (1.24)$$

According to Prop. 1.1 and adopting the damage law (1.11) (a stress softening law) the strain-damage homogeneous configuration is *invariant* with respect to the bar length: what varies is its stability. For short bars, defined by $L < \lambda_{cr}\ell$, exists an interval of imposed displacement for which the damaging homogeneous phase is stable (i.e. the damage rate α_t grows uniformly $\forall x \in \Omega$, satisfying (1.23d)):

$$\begin{cases} L < \lambda_{cr}\ell \text{ (short bar)} \\ U_t \in [U_e, U_{cr}] \end{cases} \longrightarrow \text{homogeneous solution is stable} \left(U_{cr} = \frac{\lambda_{cr}U_e\ell}{L} \right), \quad (1.25)$$

where U_{cr} is the *critical imposed displacement* on $x = L$. For long bars, defined by $L > \lambda_{cr}\ell$, the inequality (1.24) is not fulfilled for any $U_t \geq U_e$: during the damaging phase, the homogeneous configuration is *always* unstable.

Critical time

Knowing that the imposed displacement for a generic time $t \in I$ is $U_t = L \cdot t$, the critical imposed displacement can be expressed as:

$$U_{cr} = L \cdot t_{cr} \implies t_{cr} = \frac{U_{cr}}{L}, \quad (1.26)$$

where t_{cr} is defined as *critical*, i.e. the time when the damaging phase stability status changes. According to (1.25):

$$t_{cr} = \frac{U_{cr}}{L} = \frac{\lambda_{cr}U_e\ell}{L^2} = \frac{\lambda_{cr}\ell}{L^2} L \frac{\sigma_M}{E_0} = \frac{\lambda_{cr}\ell}{L} \sqrt{\frac{w_1}{E_0}} \quad (1.27)$$

1.3 Algorithm structure and numerical discretization

In this section is shown the spatio-temporal discretization procedure necessary to resolve *in silicio* the proposed quasi-static evolution problem.

As shown in [Lancioni and Royer-Carfagni \(2009\)](#) and [Pham et al. \(2011\)](#), the numerical algorithm consists of an **alternate minimization** of the energy functional with respect of the two unknown fields. Specifically:

- Definition of geometrical and physical parameters;
- Spatio-temporal domain discretization;
- Problem initialization: initial conditions

$$\alpha_{t=0}(x) = 0, \quad u_{t=0}(x) = 0, \quad \forall x \in \Omega$$

- For $t = \Delta t, 2\Delta t, \dots, t_{\text{fin}}$:

$$u_t = \underset{u \in \mathcal{C}(U_t)}{\operatorname{argmin}} \mathcal{P}(u, \alpha_{t-1}), \quad \text{under the constraints} \quad \begin{cases} u_t(x=0) = 0 \\ u_t(x=L) = U_t = Lt \end{cases} \quad (1.28)$$

$$\alpha_t = \underset{\alpha \in \mathcal{D}_1}{\operatorname{argmin}} \mathcal{P}(u_t, \alpha), \quad \text{under the constraint} \quad \alpha_t(x) \geq \alpha_{t-1}(x), \quad \forall x \in \Omega \quad (1.29)$$

- Post-processing actions.

The operations (1.28) and (1.29), repeated $\forall t_i \in I_i$ (where I_i is the discrete time domain), represent the algorithm core: their operative forms are obtained and reported as shown in the subsequent subsections.

1.3.1 \mathcal{P} minimization form with respect to u

As reported in [Li et al. \(2017\)](#), one of the possible formulations to express the variational problem (1.7) (under satisfied regularity conditions on \mathcal{P} , u and α) is the *minimization form*, which expression with respect to u is:

$$\begin{aligned} \min_{v \in V} \mathcal{P}_{\bar{\alpha}}(v), \quad \mathcal{P}_{\bar{\alpha}}(v) &= \int_0^L \left[\frac{1}{2} E(\bar{\alpha}) v'^2 + \left(w(\bar{\alpha}) + \frac{1}{2} w(1) \ell^2 \bar{\alpha}'^2 \right) v \right] dx \\ \implies \mathcal{P}_{\bar{\alpha}}(v) &= \frac{1}{2} E(\bar{\alpha}) \int_0^L v'^2 dx + \int_0^L f v dx, \end{aligned} \quad (1.30)$$

where $f = w(\bar{\alpha}) + \frac{1}{2} w(1) \ell^2 \bar{\alpha}'^2$ denotes the *constant term* (with fixed $\alpha = \bar{\alpha} = \alpha_{t-1}$) and $V = \mathcal{C}_0(U_t) = \{v \in \mathcal{C}(U_t) : v(0) = 0\}$.

To express the solution field numerically, it is necessary to introduce a *finite dimensional space* $V_h \subset V$, defined by a set of basis function:

$$V_h = \text{span} \{ \phi_1, \dots, \phi_{N-1} \}, \quad (1.31)$$

where N is the number of spatial nodes that define the discretization. One of the most common and adaptable approximation *polynomial* space is formed by the so-called *La-grangian* or *hat functions*:

$$\phi_j(x) = \begin{cases} \frac{x-x_{j-1}}{h_j} & \text{for } x \in [x_{j-1}, x_j] \\ \frac{x_{j+1}-x}{h_{j+1}} & \text{for } x \in [x_j, x_{j+1}] \\ 0 & \text{elsewhere} \end{cases} \quad (1.32)$$

Using this approximation method, the numerical solution expression takes the form:

$$\begin{aligned} u_h(x) &= \sum_{j=1}^{N-1} p_j \phi_j(x) \\ \Rightarrow \mathcal{P}_{\bar{\alpha}}(u_h) &= \frac{1}{2} E(\bar{\alpha}) \int_0^L \left(\sum_{j=1}^{N-1} p_j \phi_j'(x) \right)^2 dx + \int_0^L f \cdot \left(\sum_{j=1}^{N-1} p_j \phi_j(x) \right) dx \end{aligned} \quad (1.33)$$

The functional approximate form can be interpreted as a *multivariate function* with respect to the Lagrangian coefficients p_j :

$$\mathcal{P}_{\bar{\alpha}}(u_h) = \mathcal{P}_{\bar{\alpha}}(p_1, p_2, \dots, p_{N-1}) \quad (1.34)$$

Hence, a necessary condition for a functional minimum is:

$$\frac{\partial \mathcal{P}_{\bar{\alpha}}}{\partial p_i} = 0, \quad i = 1, \dots, N-1 \quad (1.35)$$

Imposing the minimum condition $\forall i$ the following linear system is obtained:

$$\begin{aligned} \frac{\partial \mathcal{P}_{\bar{\alpha}}}{\partial p_i} &= \sum_{j=1}^{N-1} \left[\left(\int_0^L E(\bar{\alpha}(x)) \phi_j'(x) \phi_i'(x) dx \right) p_j \right] + \int_0^L f \phi_i dx = 0, \quad i = 1, \dots, N-1 \\ \Rightarrow \sum_{j=1}^{N-1} A_{ij} \cdot p_j + f_i &= 0, \quad i = 1, \dots, N-1 \\ \Rightarrow \mathbf{A} \mathbf{p} + \mathbf{f} &= 0 \end{aligned} \quad (1.36)$$

It is important to note that for problem (1.7) this approximation method (also called *Ritz method*) brings to the same results achieved by the *Galerkin* discretization scheme.

Regarding (1.36), the vector $\mathbf{p} \in \mathbb{R}^N$ represents the problem unknown, containing the Lagrangian coefficients that, for a generic $t \in I$, compose the displacement approximate form u_h . The element $\mathbf{A} \in \mathbb{R}^{N \times N}$ is the *diffusion numerical matrix*. According to the (1.11) damage law assumption, the generic element A_{ij} can be written as:

$$A_{ij} = \int_0^L [E(\bar{\alpha}) \phi_j' \phi_i'] \circ (x) dx = E_0 \int_0^L [(1 - \bar{\alpha})^2 \phi_j' \phi_i'] \circ (x) dx \quad (1.37)$$

Owing to the chosen set of basis function (1.32), the diffusion numerical matrix consists in:

$$A_{ij} = \begin{cases} \frac{\mu^-}{x_{i+1}-x_i} + \frac{\mu^+}{x_{i+2}-x_{i+1}} & \text{for } j = i \\ -\frac{\mu^+}{x_{i+2}-x_{i+1}} & \text{for } j = i \pm 1 \\ 0 & \text{elsewhere} \end{cases}, \quad \begin{cases} \mu^- = \frac{E(\bar{\alpha}(x_{i+1})) + E(\bar{\alpha}(x_i))}{2} \\ \mu^+ = \frac{E(\bar{\alpha}(x_{i+2})) + E(\bar{\alpha}(x_{i+1}))}{2} \end{cases} \quad (1.38)$$

It is clear that \mathbf{A} is a *tridiagonal* and *symmetric* matrix.

1.3.2 \mathcal{P} minimization form with respect to α

In this case, starting from (1.10), applying the damage law (1.11) and fixing $u = \bar{u} = u_t$:

$$\begin{aligned} \mathcal{P}_{\bar{u}}(\alpha) = & \underbrace{\int_0^L \left(\frac{1}{2} w(1) \ell^2 \right) \alpha'^2 dx}_{\text{diffusive term}} + \underbrace{\int_0^L (w(1) - E_0 \bar{u}^2) \alpha dx}_{\text{reactive term}} + \\ & + \underbrace{\int_0^L \frac{1}{2} E_0 \bar{u}^2 dx}_{\text{constant term}} + \underbrace{\int_0^L \left(\frac{1}{2} E_0 \bar{u}^2 \right) \alpha^2 dx}_{\text{quadratic term}} \end{aligned} \quad (1.39)$$

As evidenced in (1.39), a *quadratic term* in the energy functional \mathcal{P} expressed with respect to the damage variable α is present. Hence, the Ritz-Galerkin approximation method application is not possible. To minimize $\mathcal{P}_{\bar{u}}$ a bound-constrained quadratic optimization MATLAB® tool is implemented, as focused in Subsect. 1.4.2.

1.4 MATLAB® code analysis

In the following section the primary parts of the solving MATLAB® code are shown and analyzed, starting from the `main` function and then focusing on various implemented subfunctions, one each intended to reach a specific sub-task.

1.4.1 main and DiffusionAssembler function

The `main` is the starting and controlling point of the program execution, containing all the physical definition and initialization parameters, as well as the subfunctions recalls. As shown in Sect. 1.3, the program core is represented by the temporal `for` loop:

Listing 1.1: `main` function: `for` loop over time discretization

```

1 for t=t_in:delta_t:t_fin
2   %% ALTERNATE MINIMIZATION ALGORITHM %%
3   % Ist part: minimization with resp. to u variable → linear system
      resolution
4
5   % Diffusion numerical matrix assembly:
6   A = DiffusionAssembler(E,x,alpha);
7   % Constant term assembly (in his homogeneous form, Au = 0):
8   B = ConstantTermAssembler(f,x,alpha,alphapr);
9   % Non-homogeneous Dirichlet cond.s (f != 0) → constant term correction:
10  B = DirichletNonOmo(B,x,E,alpha);
11  % Linear system resolution:
12  u = A\B;
13  % Displacement first derivative evaluation:
14  upr = DisplDerivate(u,x);
15
16
17  % IInd part: minimization with resp. to damage var. → bound-constrained
      quadratic optimization solver
18  alpha = minalpha(upr,x,alpha);
19  % Damage field first derivative evaluation:
20  alphapr = DamageDerivate(alpha,x);
21
22  % post-processing
23  [v_alpha,max_alpha,sigma_t,i] = PostProc(alpha,i,upr,v_alpha,max_alpha,
      sigma_t);
24  [E_Diss,E_El] = DissEnergy(E_Diss,E_El,alpha,sigma_t,i);
25 end

```

As observed in line 1 of the `main` function, the time domain discretization consists of an uniform step (equals to `delta_t`) configuration. Instead, the spacial discretization is a non-uniform grid using *Chebyshev nodes*, that minimize the effect of *Runge's phenomenon*

for polynomial interpolation, as investigated in [Stewart \(1996\)](#).

The function `DiffusionAssembler` traces operatively the theoretical results reported in Eq. (1.38).

Listing 1.2: `DiffusionAssembler` function structure

```

1 function A = DiffusionAssembler(E,x,alpha)
2
3 % function to assembly the diffusion numerical matrix A
4 %%% INPUT %%%
5 %     E : damage law function (E = @(a) E_0*(1 - a).^2)
6 %     x : spacial discrete domain
7 %     alpha : code equivalent to \bar{\alpha} := \alpha_{t-1}
8
9 global N
10 A = zeros(N,N);
11
12 E = E(alpha);
13
14 for i=1:N
15     pmm = (E(i+1) + E(i))/2;
16     pmp = (E(i+2) + E(i+1))/2;
17     A(i,i) = A(i,i) + (pmm)/(x(i+1) - x(i)) + (pmp)/(x(i+2) - x(i+1));
18     if i ~= N
19         A(i,i+1) = A(i,i+1) - (pmp)/(x(i+2) - x(i+1));
20         A(i+1,i) = A(i,i+1);
21     end
22 end
23 end

```

1.4.2 minalpha function

The function `minalpha` outputs the vector `alpha` of $[1, N+2]$ dimension (N is the number of the *internal* spatial nodes) coming from the numerical minimization of the functional integral in its discrete form (as shown in line 19-28 code section). As displayed in line 21-23, the numerical functional evaluation is performed through a II^{nd} -order *centered finite difference scheme* (essential to estimate the $[\alpha'(x)]^2$ expression in the diffusive term):

$$\alpha'(x_{j+1}) = \frac{\alpha(x_{j+2}) - \alpha(x_j)}{x_{j+2} - x_j} + O(\Delta x^2), \quad \Delta x = x_{j+1} - x_j \quad (1.40)$$

Another important code section is related to the physical (i.e. damage irreversibility) and constitutive constraint imposed on the damage field. Theoretically, these conditions are expressed by the functional spaces (1.8) and (1.5b), respectively. The irreversibility condition (as reported in [Lancioni and Royer-Carfagni \(2009\)](#)) is fulfilled by simply imposing:

$$\alpha_t(x_j) \geq \alpha_{t-1}(x_j), \quad \forall j \in [1, N+1] \quad (1.41)$$

In the code, this imposition is operated in line 9-14. The constitutive constraint is actuated in line 31-34, by bounding the maximum and minimum value that `alpha` can assume.

Listing 1.3: `minalpha` function structure

```

1 function alpha = minalpha(upr,x,alpha)
2 global w1 E0 l N
3
4 % new alpha definition
5 old_alpha = alpha;
6 alpha = optimvar('alpha',1,N+2);
7
8 % irreversibility condition implementation
9 irr_cond = false(1,N+2);
10 for j = 2:N+1
11     irr_cond(1,2:j-1) = false;
12     irr_cond(1,j) = true;
13     alpha.LowerBound(irr_cond) = old_alpha(j);
14 end
15
16 funct_alpha = optimexpr(1,N+2);
17
18 % P(alpha) evaluation for every internal spatial node
19 for j = 1:N
20
21     funct_alpha(j) = funct_alpha(j) + 0.5*w1*(l^2).*(((alpha(j+2))-...
22         alpha(j))./(x(j+2)-x(j))))).^2 + (w1 - E0*(upr(j)).^2).*alpha(j+1)+...
23         0.5*E0*(upr(j)).^2 + 0.5*E0.*(alpha(j+1)).^2.*(upr(j)).^2;
24
25 end
26
27 % functional integral evaluation → sum all over the spatial domain
28 alphaproblem = optimproblem('Objective',sum(funct_alpha));
29
30 % Constitutive constraint: 0 <= alpha <= 1
31 htcons1 = alpha <= 1;
32 htcons2 = alpha >= 0;
33 alphaproblem.Constraints.htcons1 = htcons1;
34 alphaproblem.Constraints.htcons2 = htcons2;
35
36
37 alpha = solve(alphaproblem);
38 end

```

1.5 Simulation results

In the following section numerical results are reported, focusing on two geometries (a *long* and a *short bar*). The goal is to underline (as pointed out in Subsect. 1.2.3) the nature of the characteristic length ℓ for the mechanical behavior during homogeneous damage processes. The common parameters choices are:

$$\text{Discretization parameters: } \begin{cases} N = 100 \text{ (number of spatial nodes)} \\ N_t = 100 \text{ (number of temporal divisions)} \\ t \in I, I = [0, 2t^*], t^* : \text{transition time (def. in (1.18))} \end{cases} \quad (1.42a)$$

$$\text{Physical parameters: } \begin{cases} E_0 = 29 \cdot 10^9 \text{ N/m}^2 \\ w_1 = 698 \text{ N/m}^2 \\ \ell = 38 \cdot 10^{-3} \text{ m} \end{cases} \quad (1.42b)$$

Recalling (1.18), the *transition time* t^* is:

$$t^* = \frac{U_e}{L} = \sqrt{\frac{w_1}{E_0}} \approx 1.5514 \cdot 10^{-4} \quad (1.43)$$

The bar length L values selected to distinguish the two different mechanical performances are:

Long bar: $L = 2\lambda_{cr}\ell \approx 180 \cdot 10^{-3} \text{ m}$;

Short bar: $L = \lambda_{cr}\ell/2 \approx 46 \cdot 10^{-3} \text{ m}$.

For data evaluation, normalized independent variables $\tilde{x} = x/L$ and $\tilde{t} = t/t^*$ are considered (hereinafter, $\tilde{x} = x$ and $\tilde{t} = t$ for simplicity sake).

The evaluated physical quantities are: the damage field α as a function of x and t ; the maximum α computed value on $x \in [0, L]$ with respect of t ; the normalized stress σ_t/σ_M with respect of t ; the elastic and dissipated energy due to the fracture during the process.

1.5.1 Damage field $\alpha(x, t)$

In this subsection α plots are shown: in Fig. 1.2 as a function of the spatial and temporal variables, whereas in Fig. 1.3 the maximum computed α values in $\Omega, \forall t \in I$ are considered. For $t < 1$ the damage status remains null, expressing the elastic phase course. For $t > 1$:

Long bar: As disclosed in Sect 1.2.3, the homogeneous damaging configuration is *always* unstable for $L > \lambda_{cr}\ell$: this can be seen observing the abrupt $[\max(\alpha)](t)$ growth in Fig. 1.3.

Short bar: Initially, the damage variable growth is clearly smoother. This is justifiable pointing out that for $L < \lambda_{cr}\ell$ exists a time interval $[t^*, t_{cr}]$ such that the homogeneous damaging configuration is stable. Approaching $t = 2$, the damage begins to strongly localize: this is a classical unstable damaging evolution feature, implying that the system stability status is changed (from *stable* to *unstable*).

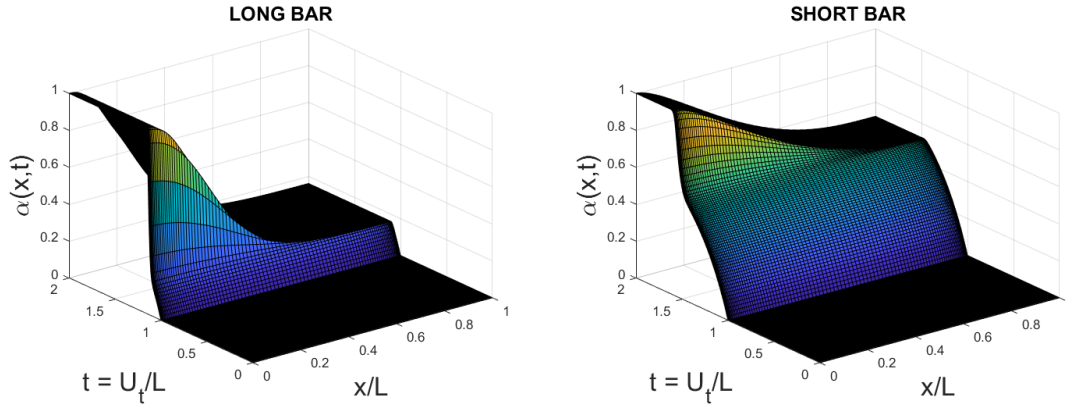


Figure 1.2: Damage field $\alpha(x,t)$ plot. Simulation data capture the main difference between the two cases: the *transition smoothness* between the elastic and the damage phase, as explained in Sect. 1.2.2 and 1.2.3.

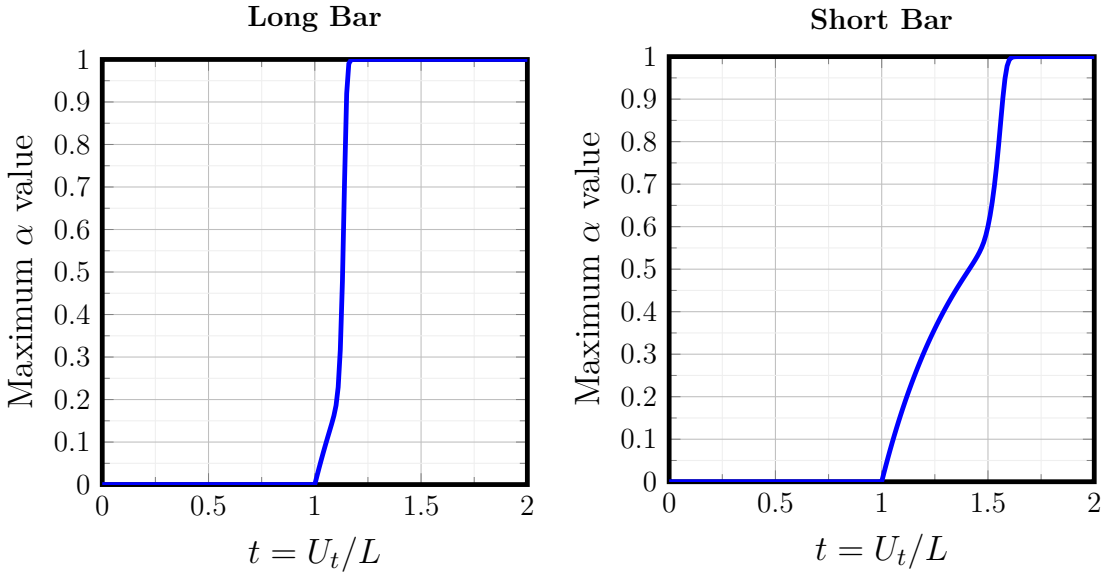


Figure 1.3: Maximum $\alpha_t(x)$ plot over t . The *transition smoothness* difference is caught also in this graphs.

1.5.2 Stress σ_t

In Fig. 1.4 the uniform stress σ_t is reported versus time for the two length cases: for both there is a sharp trend change for $t > t^*$. For the long bar case, the stress drops to zero due to the immediate damage instability. For the short bar case, for $t^* < t < t_{cr}$, the stress follows the theoretical trend reported in (1.23c) (for $U_t \geq U_e$, i.e. the stable

damaging phase). On the other hand, for $t < t^*$, the mechanical behavior is the same and it corresponds to an *elastic response*, as stated in (1.23c) (for $U_t < U_e$).

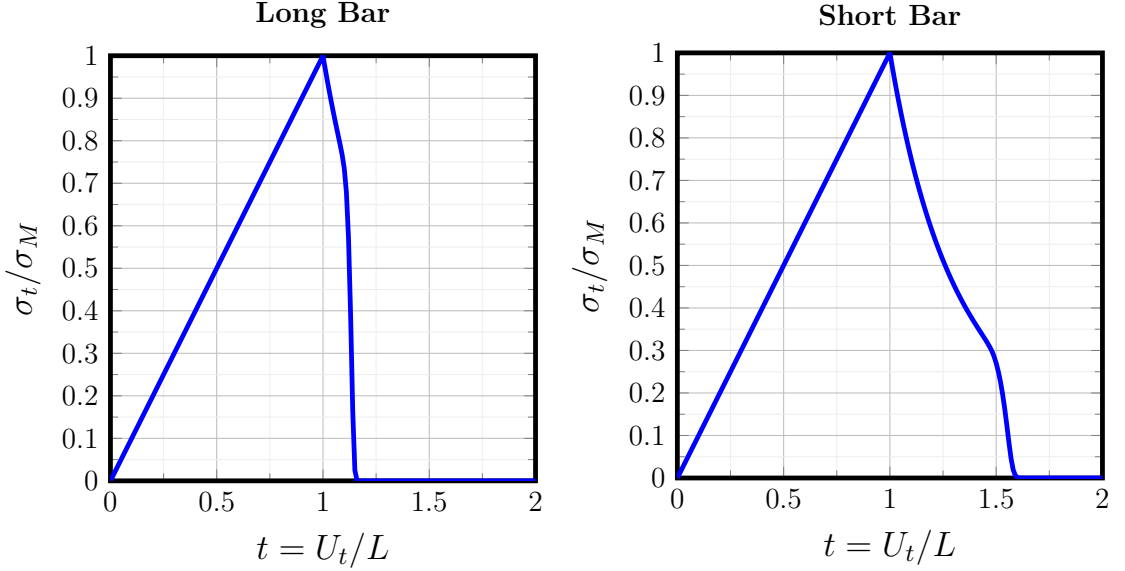


Figure 1.4: Uniform stress σ_t plot. In both cases there is a sharp trend change for $t > t^*$. For the long bar case, the stress drops to zero due to the immediate damage instability emergence. For the short bar case, for $t^* < t < t_{cr}$, the stress follows the theoretical trend reported in (1.23c) (i.e. the stable damaging phase).

1.5.3 Elastic energy E_{el}

In Fig. 1.5 the normalized *elastic energy* results are shown, computed as reported in Pham et al. (2011):

$$E_{el} = \left(\frac{1}{G_c \sqrt{C}} \right) \frac{1}{2} \frac{\sigma_t^2}{E_0} L, \quad G_c = \frac{8}{3} w_1 \ell, \quad C = \frac{1}{2} \quad (1.44)$$

The simulation results show clearly that for $t < 1$ the energy trend is *quadratic* for both cases. For $t > 1$: for the long bar, the energy drop is sudden, due to the *unstable damaging phase* outbreak; for the short bar, the energy decrease is initially smooth, according to the *stable damaging phase* development.

1.5.4 Dissipated energy E_{diss}

In Fig. 1.6 are displayed the normalized *fracture dissipated energy* plots, evaluated always starting from the Pham et al. (2011) definition:

$$E_{diss} = \left(\frac{1}{G_c \sqrt{C}} \right) \int_0^L 2w(\alpha(x)) dx = \left(\frac{1}{G_c \sqrt{C}} \right) \int_0^L 2w_1 \alpha(x) dx \quad (1.45)$$

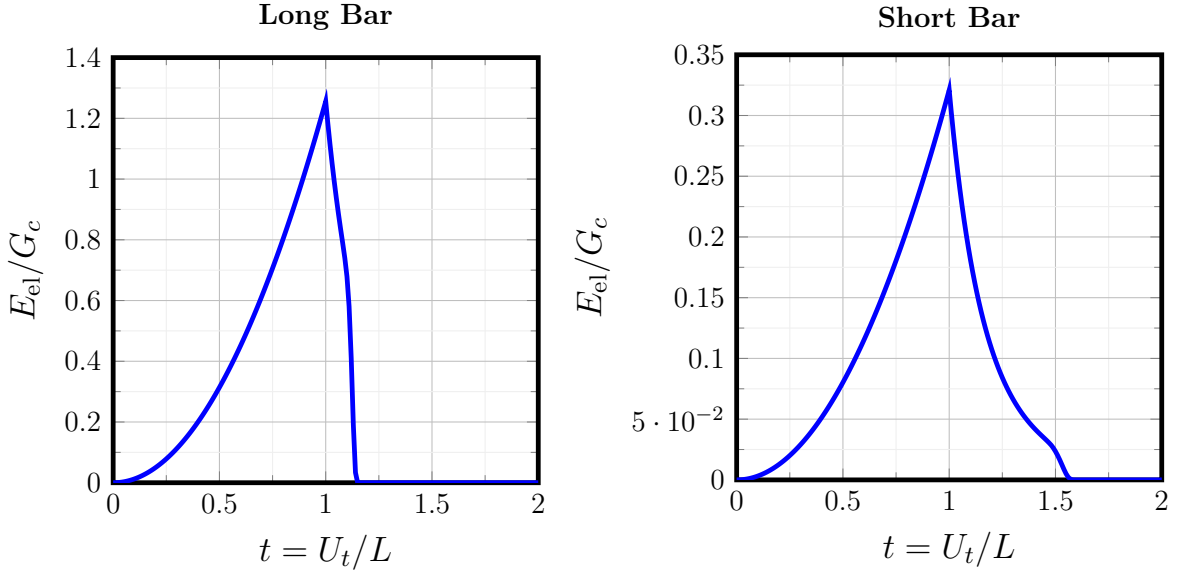


Figure 1.5: Elastic energy E_{el} plot. During elastic phase, the material absorbs energy in a quadratic manner. For $t > 1$, the elastic energy decrease differs according to the stable damaging phase presence.

For $t < 1$ (i.e. elastic phase) the dissipated energy remains null: the material is still intact. For $t > 1$, similarly to the other considered physical quantities, the dissipated energy growth changes according to the damage evolution stability: for the long bar the damage phase is unstable from the beginning, so the E_{diss} positive trend is very pronounced; for the short bar a time interval $[t^*, t_{cr}]$ exists such that the damage variable α grows *uniformly* all over the spatial domain (i.e. damaging stable configuration) and that is evidently proved also by the smooth and continuous dissipated energy trend.

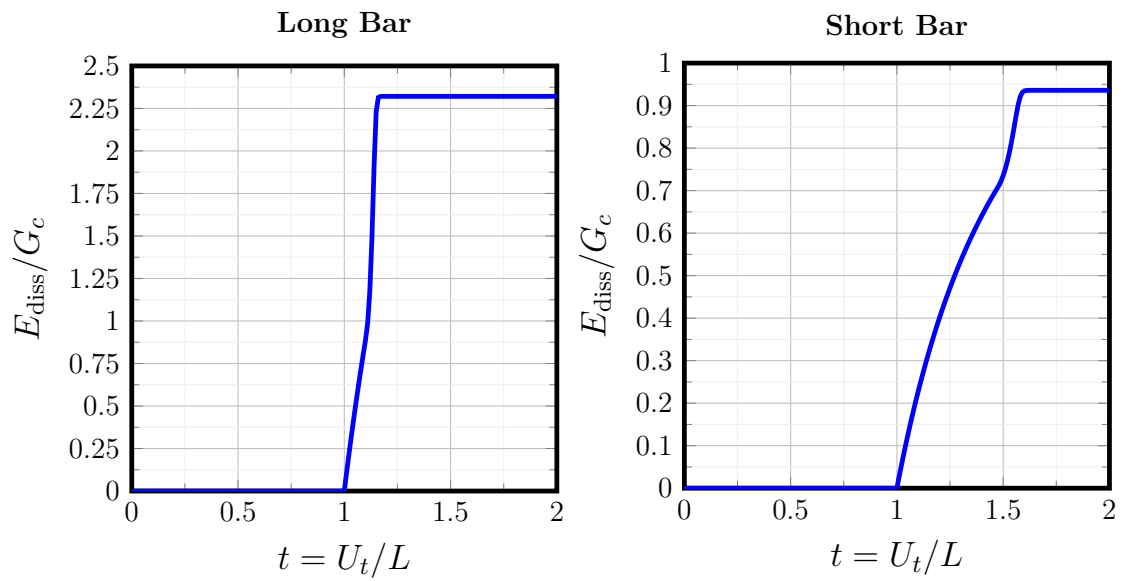


Figure 1.6: Fracture dissipated energy E_{diss} plot. For $t < 1$, during the elastic phase, the energy is null because the material is still unbroken. For $t > 1$, the energy growth trend changes depending on the fracture process stability status.

Chapter 2

Phase-Field fracture modelling: theoretical and computational features for 2D domains

It is noteworthy to mention that dealing with domains $\Omega \subset \mathbb{R}^2$ allows to validate numerical simulations with experimental data available in the literature. In this chapter the main differences between 1D and 2D fracture mechanics problems are investigated: some theoretical attributes already discussed in the previous section will be deepened and the main numerical tools (such as Abaqus/FORTRAN subroutine coupling) will be analysed.

2.1 Theoretical notes

The conceptual framework of this chapter is based on the works by [Martínez-Pañeda et al. \(2018\)](#) and [Navidtehrani et al. \(2021\)](#), where Abaqus capacity to work with FORTRAN subroutines support was exploited.

The renovated energy functional expression is:

$$\mathcal{P}(\mathbf{u}, \alpha) = \mathcal{P}^{\text{el}}(\mathbf{u}, \alpha) + \mathcal{P}^{\text{fr}}(\alpha), \quad (2.1)$$

where \mathcal{P}^{el} represents the elastic energy term (it is simply the 2D generalization of the elastic part (1.10) with the same degradation law defined in (1.11))⁴:

$$\mathcal{P}^{\text{el}}(\mathbf{u}, \alpha) = \int_{\Omega} g(\alpha) \cdot \psi_0(\boldsymbol{\varepsilon}(\mathbf{u})) \, d\Omega = \int_{\Omega} \left[(1 - \alpha)^2 + k \right] \cdot \left[\frac{1}{2} \boldsymbol{\varepsilon}^T \mathbb{A}_0 \boldsymbol{\varepsilon} \right] \, d\Omega \quad (2.2)$$

⁴The only formal difference is the *well-conditioning parameter* $k = 10^{-7}$, used to keep the equations system stable even for the partly-broken configurations.

and where \mathcal{P}^{fr} refers to the fracture energy term:

$$\mathcal{P}^{\text{fr}}(\alpha) = \int_{\Omega} G_c \gamma(\alpha, \nabla \alpha) \, d\Omega = \int_{\Omega} \frac{G_c}{2\ell} [\alpha^2 + \ell^2 \nabla \alpha \cdot \nabla \alpha] \, d\Omega \quad (2.3)$$

Let us remind that G_c is the material *critical energy release rate*, defined firstly in Griffith's theory as the demanded energy to create the unit crack surface. The function $\gamma(\alpha, \nabla \alpha)$ is the *crack surface density*:

$$\Gamma(\alpha) = \int_{\Omega} \gamma(\alpha, \nabla \alpha) \, d\Omega, \quad (2.4)$$

where $\Gamma \subset \mathbb{R}^{n-1}$ is the *crack surface*.

The mathematical model theoretical substrate is *slightly different* from the one used in Chapter 1 (see (1.10) and (1.11)) mainly for the new local fracture dissipation factor definition (i.e. the Π^{nd} term in (1.4)). In fact it is *quadratically* dependent with respect to the damage variable in (2.3), whereas its definition is linear in (1.11). As shown in Miehe et al. (2010), to demonstrate the new model version consistency, it is useful to start from some considerations about an intrinsic feature of the phase-field methods: the crack smooth representation.

2.1.1 Fracture smooth topology: a quadratic local energy term justification

The phase-field method basic concept is to describe crack formation and propagation smoothly, significantly reducing the computational complexity of the problem.

Defining a 1D fracture steady problem ($\Omega = \mathbb{R}$, crack in $x = 0$), the phase-field theory allows us to change representation, as also shown in Fig. 2.1:

$$\underbrace{\begin{cases} \alpha(x) = 1 & \text{for } x = 0 \\ \alpha(x) = 0 & \text{elsewhere} \end{cases}}_{\text{Sharp crack representation}} \implies \underbrace{\alpha(x) = e^{-\frac{|x|}{\ell}}}_{\text{Smooth crack representation}} \quad (2.5)$$

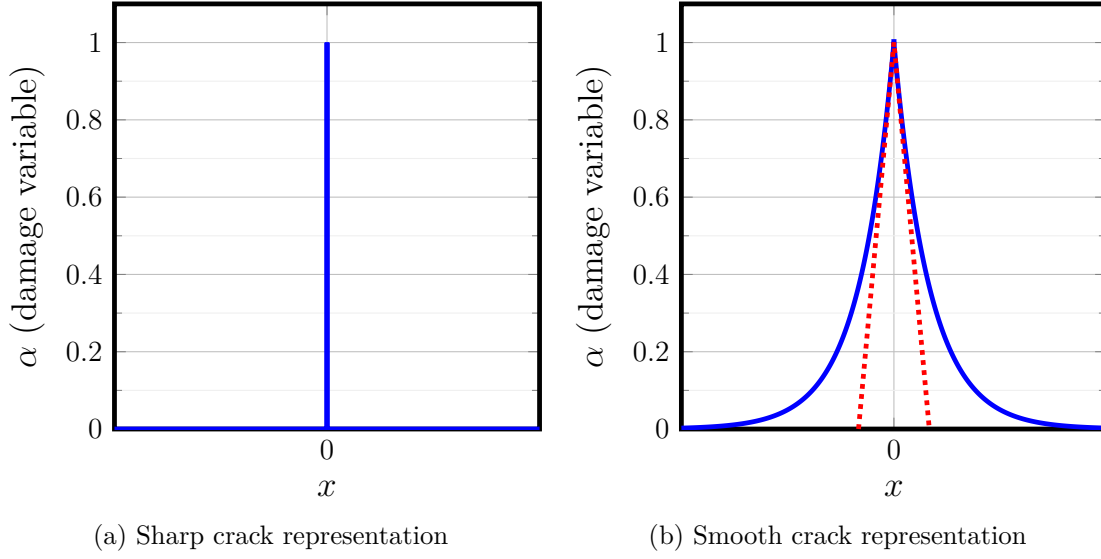


Figure 2.1: Two topology strategies to model 1D fracture.

The length parameter ℓ defines how much the *crack zone width* (physically interpretable as the continuum region involved in the nano voids appearance that follows the crack formation) extends.

The exponential model equation in (2.5) is the solution of the following Cauchy problem:

$$\ell^2 \frac{d^2 \alpha}{dx^2} - \alpha = 0 \quad \text{in } \mathbb{R}, \quad \alpha(0) = 1 \vee \alpha \rightarrow 0 \text{ for } x \rightarrow \pm\infty \quad (2.6)$$

Expressing the problem in weak form, we have:

$$\int_{\mathbb{R}} (\ell^2 \alpha'' v - \alpha v) dx = 0, \quad \forall v \in V, \quad V = \left\{ v \in L^2(\Omega) : v(0) = 1 \vee v \rightarrow 0 \text{ for } x \rightarrow \pm\infty \right\}, \quad (2.7)$$

and applying integration by parts yields:

$$\int_{\mathbb{R}} (\ell^2 \alpha' v' + \alpha v) dx = 0 \quad (2.8)$$

Dealing with Eq. (2.8) corresponds to solve the variational problem:

$$\inf_{\alpha \in V} I(\alpha), \quad I(\alpha) = \int_{\mathbb{R}} \left[\alpha^2 + \ell^2 \left(\frac{d\alpha}{dx} \right)^2 \right] dx \quad (2.9)$$

The damage variable $\alpha(x)$ exponential form inserted in the functional $I(\alpha)$ gives:

$$I(\alpha(x) = e^{\frac{-|x|}{\ell}}) = \int_{\mathbb{R}} \left[e^{\frac{-2|x|}{\ell}} + \ell^2 \left(-\frac{\text{sgn}(x)}{\ell} e^{\frac{-|x|}{\ell}} \right)^2 \right] dx = \int_{\mathbb{R}} 2e^{\frac{-2|x|}{\ell}} dx = 2\ell \quad (2.10)$$

At this point if we expand the problem dimensions such that $\Omega \subset \mathbb{R}^n$ and the spatial integration is made on $d\Omega = \Gamma dx$ (with $\Gamma \subset \mathbb{R}^{n-1}$ representing the *crack extension*):

$$I(\alpha) = \Gamma \cdot 2\ell \implies \Gamma = \frac{1}{2\ell} \cdot I(\alpha) \quad (2.11)$$

This latter equation defines a *crack density* for unit length. To derive the *crack energy density* expression it is sufficient to add the critical energy release rate G_c as multiplier:

$$\mathcal{P}^{\text{fr}}(\alpha) = \frac{G_c}{2\ell} \cdot I(\alpha) = \int_{\Omega} \frac{G_c}{2\ell} [\alpha^2 + \ell^2 \nabla \alpha \cdot \nabla \alpha] d\Omega \quad (2.12)$$

It should be noted that Eqs. (2.3) and (2.12) are formally identical and they can be derived from the general model (1.3) imposing:

$$w(\alpha) = \alpha^2 \implies c_w = \int_0^1 \sqrt{w(\alpha)} d\alpha = \int_0^1 \alpha d\alpha = \frac{1}{2}, \quad C = 1 \quad (2.13)$$

2.1.2 AT1 and AT2 fracture modelling

As said before, the main difference between the two analyzed approaches can be attributed to the local damage term modelling:

$$\mathcal{P}_{\text{local},1}^{\text{fr}}(\alpha) := \mathcal{P}_{\text{AT1}} = w_1 \alpha = \frac{3G_c}{8\ell} \alpha, \quad (2.14a)$$

$$\mathcal{P}_{\text{local},2}^{\text{fr}}(\alpha) := \mathcal{P}_{\text{AT2}} = \frac{G_c}{2\ell} \alpha^2 \quad (2.14b)$$

The two models (hereinafter called AT1 and AT2 respectively) have been widely implemented and studied in their strength and weakness, see [Tanné et al. \(2017\)](#) and [Pham et al. \(2011\)](#). Let us focus on AT2 properties:

Elastic phase: Confirming the stiffness degradation law $E(\alpha) = E_0(1 - \alpha)^2$ and recalling the U_e (maximum elastic displacement) expression:

$$\begin{cases} U_e = -\frac{LG_c}{2\ell} \sqrt{\frac{2w'(\alpha=0)}{E'(\alpha=0)}} \\ \frac{\partial w}{\partial x} = w'(\alpha) = 2\alpha \cdot \alpha' \end{cases} \rightarrow U_e(\text{AT2}) = 0, \quad \sigma_e(\text{AT2}) = 0 \quad (2.15)$$

Therefore AT2 model does not involve an elastic phase: damage begins to arise just when traction starts.

Peak stress: Another important changing feature is the *peak stress* value (for AT1 case, see (1.23b)):

$$\begin{aligned} \sigma_M &:= \sup_{\alpha \in [0,1]} \sqrt{\frac{2w'(\alpha)}{S'(\alpha)}} = \sup_{\alpha \in [0,1]} \sqrt{\frac{G_c \alpha (1 - \alpha)^3 E_0}{\ell}} = \\ &= \sqrt{w_1 E_0} \cdot \left(\sup_{\alpha \in [0,1]} \sqrt{2\alpha (1 - \alpha)^3} \right) = \sqrt{w_1 E_0} \cdot \frac{3\sqrt{3}}{8\sqrt{2}}, \end{aligned} \quad (2.16)$$

where the maximum is reached for $\alpha = \frac{1}{4}$. So we have:

$$\sigma_M(\text{AT1}) = \sqrt{w_1 E_0}, \quad \sigma_M(\text{AT2}) = \frac{3\sqrt{3}}{8\sqrt{2}} \sqrt{w_1 E_0} \quad (2.17)$$

Length parameter ℓ reformulation: Observing (2.17) it is clear that the numerical σ_M expressions have to yield the same outcomes to guarantee modelling consistence. In fact, recalling the physical relation gave by Irwin (1957):

$$\sigma_M = \sqrt{\frac{G_c E}{\ell_{\text{ch}}}} = \sigma_M(\text{AT1}) = \sigma_M(\text{AT2}), \quad (2.18)$$

where ℓ_{ch} refers to the material's characteristic length. So we have:

$$\text{For AT1:} \quad \sigma_M = \sqrt{w_1 E_0} = \sqrt{\frac{3G_c E_0}{8\ell}} \rightarrow \ell(\text{AT1}) := \ell_1 = \frac{3}{8} \ell_{\text{ch}} \quad (2.19a)$$

$$\text{For AT2:} \quad \sigma_M = \frac{3\sqrt{3}}{8\sqrt{2}} \sqrt{w_1 E_0} = \sqrt{\frac{27G_c E_0}{256\ell}} \rightarrow \ell(\text{AT2}) := \ell_2 = \frac{27}{256} \ell_{\text{ch}} \quad (2.19b)$$

The regularization lengths ℓ_1 and ℓ_2 can be interpreted as numerical parameters defined from ℓ_{ch} , a classical material property.

2.2 Numerical formulation

2.2.1 Balance laws weak form

To express the fracture mathematical problem in its numerical form it is useful to report the weak form of the displacement and damage variable balance equations. We start from the *virtual work principle* application:

$$\delta W_{\text{int}} = \delta W_{\text{ext}} \quad (2.20)$$

The internal work differential δW_{int} is:

$$\begin{aligned} \delta W_{\text{int}} &= \left(\frac{\partial \mathcal{P}}{\partial \boldsymbol{\varepsilon}} \right) : \delta \boldsymbol{\varepsilon} + \left(\frac{\partial \mathcal{P}}{\partial \alpha} \right) \cdot \delta \alpha, \\ \frac{\partial \mathcal{P}}{\partial \boldsymbol{\varepsilon}} &= \int_{\Omega} [(1 - \alpha)^2 + k] \cdot (\mathbb{A}_0 \boldsymbol{\varepsilon}) \, d\Omega \rightarrow \left(\frac{\partial \mathcal{P}}{\partial \boldsymbol{\varepsilon}} \right) : \delta \boldsymbol{\varepsilon} = \int_{\Omega} [(1 - \alpha)^2 + k] \cdot (\mathbb{A}_0 \boldsymbol{\varepsilon}) \delta \boldsymbol{\varepsilon} \, d\Omega \\ \frac{\partial \mathcal{P}}{\partial \alpha} &= \int_{\Omega} \left\{ -2(1 - \alpha) \psi_0(\boldsymbol{\varepsilon}) + G_c \left[\frac{\alpha}{\ell} + \frac{\ell}{2} \frac{\partial}{\partial \alpha} |\nabla \alpha|^2 \right] \right\} d\Omega \rightarrow \\ \left(\frac{\partial \mathcal{P}}{\partial \alpha} \right) \cdot \delta \alpha &= \int_{\Omega} \left\{ -2(1 - \alpha) \delta \alpha \psi_0(\boldsymbol{\varepsilon}) + G_c \left[\frac{\alpha}{\ell} \delta \alpha + \ell \nabla \alpha \cdot \nabla \delta \alpha \right] \right\} d\Omega \rightarrow \\ \delta W_{\text{int}} &= \int_{\Omega} \left\{ [(1 - \alpha)^2 + k] \cdot (\mathbb{A}_0 \boldsymbol{\varepsilon}) \delta \boldsymbol{\varepsilon} - 2(1 - \alpha) \delta \alpha \psi_0(\boldsymbol{\varepsilon}) + G_c \left[\frac{\alpha}{\ell} \delta \alpha + \ell \nabla \alpha \cdot \nabla \delta \alpha \right] \right\} d\Omega, \end{aligned} \quad (2.21)$$

whereas the external work differential δW_{ext} is:

$$\delta W_{\text{ext}} = \int_{\Omega} \mathbf{f} \cdot \delta \mathbf{u} \, d\Omega + \int_{\partial\Omega_F} \mathbf{F} \cdot \delta \mathbf{u} \, d\Gamma, \quad (2.22)$$

where \mathbf{f} and \mathbf{F} are the imposed body force and surface force fields respectively (the latter is applied on the Neumann-type boundary portion, $\partial\Omega_F$). Applying (2.20) and referring to $\boldsymbol{\sigma} = g(\alpha) \cdot \boldsymbol{\sigma}_0 = [(1 - \alpha)^2 + k] \cdot (\mathbb{A}_0 \boldsymbol{\varepsilon})$ for brevity sake:

$$\begin{aligned} & \int_{\Omega} \left\{ \boldsymbol{\sigma} \delta \boldsymbol{\varepsilon} - 2(1 - \alpha) \delta \alpha \psi_0(\boldsymbol{\varepsilon}) + G_c \left[\frac{\alpha}{\ell} \delta \alpha + \ell \nabla \alpha \cdot \nabla \delta \alpha \right] \right\} d\Omega + \\ & - \int_{\Omega} \mathbf{f} \cdot \delta \mathbf{u} \, d\Omega - \int_{\partial\Omega_F} \mathbf{F} \cdot \delta \mathbf{u} \, d\Gamma = 0 \rightarrow \\ & \rightarrow \int_{\Omega} (\boldsymbol{\sigma} \delta \boldsymbol{\varepsilon} - \mathbf{f} \cdot \delta \mathbf{u}) \, d\Omega - \int_{\partial\Omega_F} \mathbf{F} \cdot \delta \mathbf{u} \, d\Gamma + \\ & + \int_{\Omega} \left\{ -2(1 - \alpha) \delta \alpha \psi_0(\boldsymbol{\varepsilon}) + G_c \left[\frac{\alpha}{\ell} \delta \alpha + \ell \nabla \alpha \cdot \nabla \delta \alpha \right] \right\} d\Omega = 0 \end{aligned}$$

Given the arbitrariness of the admissible virtual displacements $\delta \mathbf{u}$ and damage states $\delta \alpha$, it follows that:

$$\int_{\Omega} (\boldsymbol{\sigma} \delta \boldsymbol{\varepsilon} - \mathbf{f} \cdot \delta \mathbf{u}) \, d\Omega - \int_{\partial\Omega_F} \mathbf{F} \cdot \delta \mathbf{u} \, d\Gamma = 0, \quad (2.23a)$$

$$\int_{\Omega} \left\{ -2(1 - \alpha) \delta \alpha \psi_0(\boldsymbol{\varepsilon}) + G_c \left[\frac{\alpha}{\ell} \delta \alpha + \ell \nabla \alpha \cdot \nabla \delta \alpha \right] \right\} d\Omega = 0 \quad (2.23b)$$

Equations (2.23) represent the *weak form* of the displacement and damage variable balance laws, which is the most useful expression to define the discrete formulation of the problem. Similarly to the procedure followed in Chapter 1, a *staggered approach* is implemented, splitting the crossed dependency in (2.23b) concerning $\psi_0 = \psi_0(\boldsymbol{\varepsilon})$. Martínez-Pañeda et al. (2018) introduced an *history variable field*, defined as:

$$H = \begin{cases} \psi_0(\boldsymbol{\varepsilon}) & \text{if } \psi_0(\boldsymbol{\varepsilon}) > H_t \\ H_t & \text{otherwise} \end{cases} \quad H_t = \psi_0(\boldsymbol{\varepsilon}(\mathbf{u}_t)) \quad (2.24)$$

The field $H = H(\mathbf{u}_{t+\Delta t}, \mathbf{u}_t)$ updates itself only if the computed elastic energy at the new time step $t + \Delta t$ is higher than the same energy computed at the previous time.

It should be noted that through H the *irreversibility condition* on the damage variable is enforced: the history field indeed fulfills Kuhn-Tucker conditions (see Gass and Fu (2013)).

2.2.2 Balance laws discrete form

With the purpose of solving numerically our (\mathbf{u}, α) problem, a *Newton-Raphson* method is implemented, consisting in a backward scheme (hence it is unconditionally stable). The technique appears mathematically as:

$$\begin{Bmatrix} \mathbf{u} \\ \alpha \end{Bmatrix}_{t+\Delta t} = \begin{Bmatrix} \mathbf{u} \\ \alpha \end{Bmatrix}_t + (\mathbf{K}_t)^{-1} \begin{Bmatrix} \mathbf{r}^{\mathbf{u}} \\ \mathbf{r}^{\alpha} \end{Bmatrix}_t, \quad (2.25)$$

where $\mathbf{r} = \{\mathbf{r}^u, \mathbf{r}^\alpha\}^T$ refers to the *residuals vector* and \mathbf{K}_t to the *numerical stiffness matrix*. In order to express the approximating solution, a lagrangian set of basis functions is enforced, similarly to the approach followed for the 1D study case (see (1.31) and (1.32)). Recalling that in this case $\Omega \subset \mathbb{R}^2$, numerical solutions can be expressed as:

$$\mathbf{u}_h = \sum_{j=1}^N \Phi_j(\hat{x}, \hat{y}) \mathbf{u}_j, \quad (2.26a)$$

$$\alpha_h = \sum_{j=1}^N \phi_j(\hat{x}, \hat{y}) \alpha_j \quad \left(\Phi_j = \begin{bmatrix} \phi_j(\hat{x}, \hat{y}) & 0 \\ 0 & \phi_j(\hat{x}, \hat{y}) \end{bmatrix} \right), \quad (2.26b)$$

where N is the number of element nodes and (\hat{x}, \hat{y}) represent the spatial variables for the reference configuration. For the following analyses, CPE4 elements were implemented from Abaqus 2D solid element library (see Smith (2009)): as showed in 2.2 it is a 4-node linear quadratic element for plane strain studies, whose basic functions set is:

$$\begin{aligned} \phi_1 &= \frac{1}{4} (1 - \hat{x}) (1 - \hat{y}), & \phi_2 &= \frac{1}{4} (1 + \hat{x}) (1 - \hat{y}), \\ \phi_3 &= \frac{1}{4} (1 + \hat{x}) (1 + \hat{y}), & \phi_4 &= \frac{1}{4} (1 - \hat{x}) (1 + \hat{y}) \end{aligned} \quad (2.27)$$

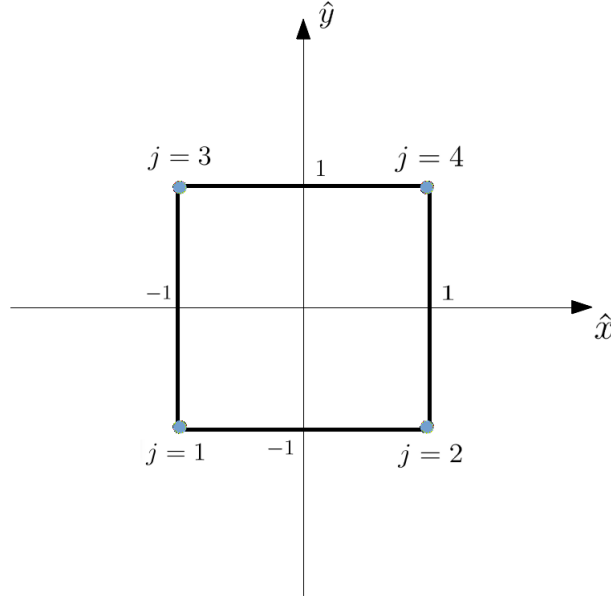


Figure 2.2: CPE4 finite element structure, based on lagrangian basic functions.

The two sets $\mathbf{u}_j = \{u_{x,j}, u_{y,j}\}$ and α_j represent the lagrangian coefficients (i.e. the unknowns). In (2.23) there are also terms dependent on derivatives of the primary variables,

so we can define:

$$\mathbf{B}_j^{\mathbf{u}} = \begin{bmatrix} \phi_{j,\hat{x}} & 0 \\ 0 & \phi_{j,\hat{y}} \\ \phi_{j,\hat{y}} & \phi_{j,\hat{x}} \end{bmatrix}, \quad \mathbf{B}_j^{\alpha} = \begin{bmatrix} \phi_{j,\hat{x}} \\ \phi_{j,\hat{y}} \end{bmatrix} \quad \left(\phi_{j,\hat{x}} = \frac{\partial \phi_j}{\partial \hat{x}}, \phi_{j,\hat{y}} = \frac{\partial \phi_j}{\partial \hat{y}} \right) \quad (2.28a)$$

$$\implies \boldsymbol{\varepsilon}_h = \sum_{j=1}^N \mathbf{B}_j^{\mathbf{u}}(\hat{x}, \hat{y}) \mathbf{u}_j, \quad (\nabla \alpha)_j = \sum_{j=1}^N \mathbf{B}_j^{\alpha}(\hat{x}, \hat{y}) \alpha_j \quad (2.28b)$$

In light of the latter reported expressions and starting from (2.23), the residuals components are enunciable as:

$$\mathbf{r}_j^{\mathbf{u}} = \int_{\Omega} \left\{ g(\alpha_t) (\mathbf{B}_j^{\mathbf{u}})^T \boldsymbol{\sigma}_0 - (\boldsymbol{\Phi}_j)^T \mathbf{f} \right\} d\Omega - \int_{\partial\Omega_F} (\boldsymbol{\Phi}_j)^T \mathbf{F} d\Gamma, \quad (2.29a)$$

$$r_j^{\alpha} = \int_{\Omega} \left\{ -2(1-\alpha) \phi_j H + G_c \left[\frac{\alpha}{\ell} \phi_j + \ell (\mathbf{B}_j^{\alpha})^T \nabla \alpha \right] \right\} d\Omega \quad (2.29b)$$

In (2.29a) the stiffness degradation function $g(\alpha) = (1-\alpha)^2 + k$ is evaluated plugging the previous time step solution ($\alpha = \alpha_t$), in order to split the crossed dependencies.

The stiffness matrix \mathbf{K} can be expressed as:

$$\mathbf{K} = \begin{bmatrix} \mathbf{K}^{\mathbf{u}\mathbf{u}} & \mathbf{K}^{\mathbf{u}\alpha} \\ \mathbf{K}^{\alpha\mathbf{u}} & \mathbf{K}^{\alpha\alpha} \end{bmatrix}, \quad (2.30a)$$

$$K_{ij}^{\mathbf{u}\mathbf{u}} = \frac{\partial \mathbf{r}_i^{\mathbf{u}}}{\partial \mathbf{u}_j} = \int_{\Omega} \left\{ g(\alpha_t) (\mathbf{B}_i^{\mathbf{u}})^T \mathbb{A}_0 \mathbf{B}_j^{\mathbf{u}} \right\} d\Omega \quad (2.30b)$$

$$K_{ij}^{\mathbf{u}\alpha} = \frac{\partial \mathbf{r}_i^{\mathbf{u}}}{\partial \alpha_j} = 0, \quad K_{ij}^{\alpha\mathbf{u}} = \frac{\partial r_j^{\alpha}}{\partial \mathbf{u}_i} = 0 \quad (2.30c)$$

$$K_{ij}^{\alpha\alpha} = \frac{\partial r_i^{\alpha}}{\partial \alpha_j} = \int_{\Omega} \left\{ \left(2H + \frac{G_c}{\ell} \right) \phi_i \phi_j + (\mathbf{B}_i^{\alpha})^T G_c \ell \mathbf{B}_j^{\alpha} \right\} d\Omega \quad (2.30d)$$

The general system showed in (2.25) can now be interpreted as:

$$\begin{cases} \mathbf{u}_{t+\Delta t} = \mathbf{u}_t + [\mathbf{K}_t^{\mathbf{u}\mathbf{u}}(\alpha_t)]^{-1} \mathbf{r}_t^{\mathbf{u}}(\alpha_t) \\ \alpha_{t+\Delta t} = \alpha_t + [\mathbf{K}_t^{\alpha\alpha}(H_t)]^{-1} \mathbf{r}_t^{\alpha}(H_t) \end{cases} \quad (2.31)$$

At this point the problem is a linear decoupled system of two equations, in which the unknowns are $(\mathbf{u}_{t+\Delta t}, \alpha_{t+\Delta t})$: the system has to be solved for each defined time step, constructing the new \mathbf{K}_t and \mathbf{r}_t from the previous time step results α_t and H_t .

2.3 Analysis definition on software

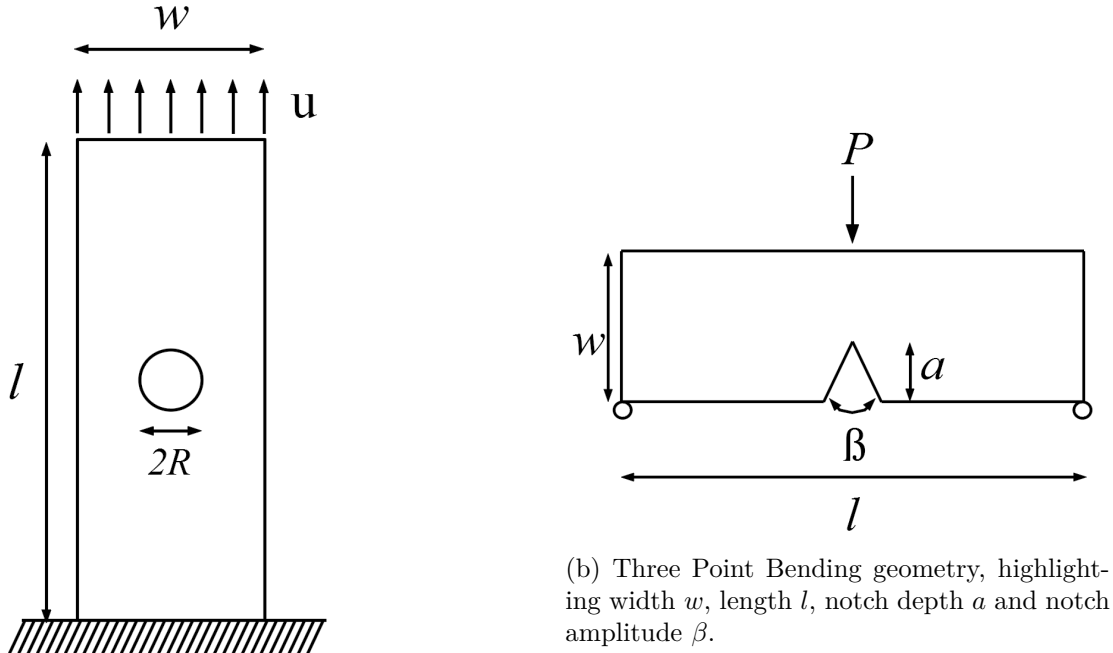
Most of FEA softwares basic releases do not implement any phase-field method applicable to fracture mechanics analysis. The following 2D simulations are carried out on Abaqus (2022 version), a Finite Element Analysis software whose greatest potentiality is to broaden its numerical functionalities through FORTRAN subroutines employment.

In this section the main model definition steps will be examined, to fully understand the computational setup on which the final results are based. To this aim, two different geometries are taken into account:

- A circular hole in an infinite tensile plate;
- A sharp V-notched sample under Three Point Bending (TPB).

In the former case, the size effect of the hole radius will be investigated by referring to the experimental work by [Sapora et al. \(2018\)](#). In the latter case, the study will focus on the influence of the notch amplitude on the failure load, as investigated in [Carpinteri \(1987\)](#).

2.3.1 Plane strain conditions and geometry



(a) Hole geometry, highlighting width w , length l and hole radius R

(b) Three Point Bending geometry, highlighting width w , length l , notch depth a and notch amplitude β .

Figure 2.3: Two geometries examples: hole geometry (see 2.3a) and Three Point Bending (TPB) geometry (see 2.3b).

The first step concerns the geometry properties definition. Simulations were performed assuming *plane strain* conditions: although the geometrical computational environment is two-dimensional, we can refer to physical circumstances in which the specimen thickness $t \neq 0$ and:

$$\varepsilon_z = \gamma_{xz} = \gamma_{yz} \approx 0 \quad (2.32)$$

$$\implies \begin{cases} \varepsilon_z = -\frac{\nu}{E}(\sigma_x + \sigma_y) + \frac{1}{E}\sigma_z = 0 \rightarrow \sigma_z = \nu(\sigma_x + \sigma_y) \\ \tau_{xz} = \frac{2(1+\nu)}{E}\gamma_{xz} = 0 \\ \tau_{yz} = \frac{2(1+\nu)}{E}\gamma_{yz} = 0 \end{cases}$$

where the σ and τ terms are the *Cauchy stress tensor* components. Assuming the hypothesis (2.32) valid, the constitutive equations takes the form:

$$\begin{cases} \varepsilon_x = \frac{1}{E}\sigma_x - \frac{\nu}{E}\sigma_y - \frac{\nu^2}{E}(\sigma_x + \sigma_y) = \frac{1}{E'}\sigma_x - \frac{\nu'}{E'}\sigma_y \\ \varepsilon_y = \frac{1}{E}\sigma_y - \frac{\nu}{E}\sigma_x - \frac{\nu^2}{E}(\sigma_x + \sigma_y) = \frac{1}{E'}\sigma_y - \frac{\nu'}{E'}\sigma_x \\ \gamma_{xy} = \frac{2(1+\nu)}{E}\tau_{xy} \end{cases} \quad \left(E' = \frac{E}{1-\nu^2} > E, \quad \nu' = \frac{\nu}{1-\nu} > \nu \right) \quad (2.33)$$

As observed in [Carpinteri \(1992\)](#) the plane strain condition is verified for prismatic solids

	Sapora et al. (2018)	Carpinteri (1987)
Length (l) [mm]	100	190
Width (w) [mm]	40	50
Thickness (t) [mm]	10 (PMMA), 8 (GPPS)	50
Geometric variables [mm]	$R = 0.25, 0.5, 1, 2$	$a = 10, 20$

Table 2.1: Specimens generic dimensions. These values refer to the entire physical geometry: the measures entered in the Abaqus model definition vary according to the specific geometry symmetry properties. R is the *hole radius* for the size effect analysis; a represents the *notch depth* for V-notch effect analysis.

(sufficiently thick⁵) subjected to loads perpendicular and independent with respect to z direction: this requirements are consistent with the analyzed study cases, as discussed in the next sections. Specimen dimensions, reported in Table 2.1, refer to the experimental tests by [Sapora et al. \(2018\)](#) and [Carpinteri \(1987\)](#).

As evidenced in Fig. 2.3 geometries' symmetry have been exploited, reducing the numerical domain area without any loss of information: for size effect of circular hole analyses, computational domains consist of the physical specimens north-west quadrant; for TPB tests only the real specimen left half has been discretized.

2.3.2 Material properties

[Martínez-Pañeda et al. \(2018\)](#) FORTRAN implemented code, involving a UEL (User-defined Element) subroutine, has a structure that suggests to define the material properties directly on the `.inp` file, modifiable with a standard text editor.

The input parameters are: the undamaged material elastic modulus E , Poisson's ratio ν , numerical characteristic length ℓ , critical energy release rate G_c and the well-conditioning parameter k . As concerns G_c , it can be evaluated according to [Irwin \(1957\)](#) relationship:

$$G_c = \frac{K_{IC}^2}{E'} = \frac{K_{IC}^2 (1 - \nu^2)}{E}, \quad (2.34)$$

⁵[Taylor \(2007\)](#) affirms that to guarantee the plane strain condition validity $t > 2.5 \ell_{ch}$ has to be fulfilled, where ℓ_{ch} is the material characteristic length. This latter property is accomplished for every considered geometry.

where K_{IC} is the *fracture toughness*, a material property that indicates the material resistance in presence of cracks. For each material, K_{IC} can be estimated following ASTM standard code.

Recalling that AT2 model is enforced, the numerical characteristic length $\ell = \ell_2$ is evaluated as:

$$\ell_2 = \frac{27}{256} \ell_{ch} \approx 0.1055 \ell_{ch} \quad (2.35)$$

It should be noted that, applying AT2 phase-field model, the calculator involves a length scale about 10 times smaller than the physical counterpart.

2.3.3 Boundary conditions

In the following all the imposed boundary condition are listed, for both analysis types.

Regarding samples containing a circular hole, only one quarter of the geometry can be modelled thanks to the double symmetry (see also Fig. 2.4):

- An YSYMM condition is imposed all over the lower side of the numerical geometry: this equals to require a symmetry with respect to a plane parallel to the y axis

$$u_y = 0, \quad \vartheta_x = 0, \quad \vartheta_z = 0, \quad (2.36)$$

where ϑ_x and ϑ_z represent the *rotational displacements* with respect to x and z axes.

- An XSYMM condition is imposed on the geometry left contour:

$$u_x = 0, \quad \vartheta_y = 0, \quad \vartheta_z = 0 \quad (2.37)$$

- In order to replicate Sapora et al. (2018) experimental setup, a displacement all over the top contour of the specimen quarter is imposed, such that the strain rate is equal to 1 mm/min.

Regarding the TPB analysis (see also Fig. 2.5):

- An XSYMM condition ((2.37)) is imposed all over the right domain side (whose length varies according to the notch amplitude β).
- A simple displacement $u_y = 0$ condition is imposed at the lower left extreme.
- A concentrated force is applied along the axis of symmetry (i.e. the specimen top central point): the imposed force rates are $CF_1 = 100N/min$ for $a = 1$ cm and $CF_2 = 50N/min$ for $a = 2$ cm.

2.3.4 Mesh generation

The mesh generation step has been approached very similarly for both cases. Observing Fig. 2.4 and 2.5 a line crosses both geometries, defining a *partition*. The internal areas (i.e. the one including the hole and the one closer to the re-entrant corner for TPB) are

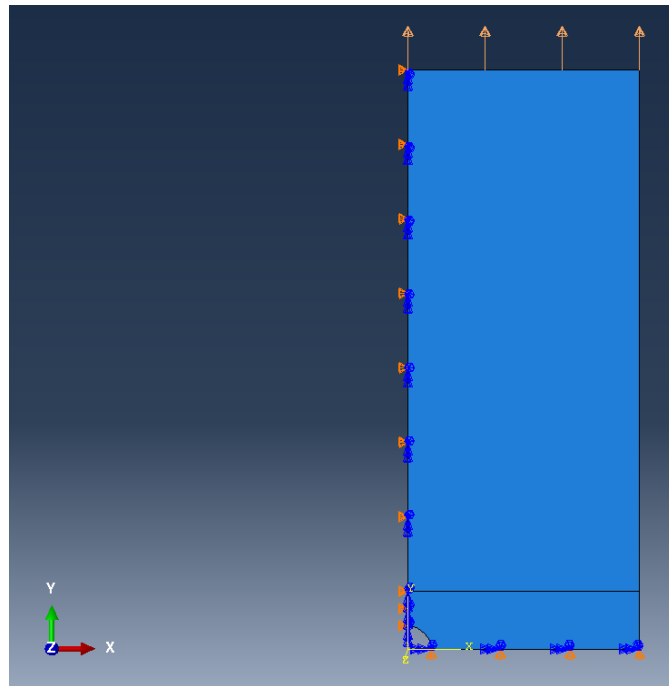


Figure 2.4: Boundary conditions for a holed geometry. A YSYMM condition on the lower contour and an XSYMM condition on the left side are imposed. The applied displacement over the top contour is also displayed.



Figure 2.5: Typical boundary condition setup on TPB samples. A XSYMM condition over the right side and a $u_y = 0$ condition on the lower contour leftmost point (circled in red) are imposed. The applied concentrated force over the top contour (circled in green) is also displayed.

characterized by the definition of a fine *free-structured* mesh, where the element minimum size $h_{\min} = \ell_2/5$ is fixed. This measure is strictly imposed all over the expected crack paths, that correspond to the bottom domain side for size effect analysis and to the right geometrical contour for TPB. Along the partition lines the element size is forced $h_{\text{part}} = \ell_2$. Coarse meshes are generated in the external areas .

An unpleasant occurrence concerns the TPB simulations. As shown in 2.7a, the fine mesh zone does not reach the top side: for simulations with a fine mesh all over the geometry right side, in fact, the material fails for very low concentrated loads.

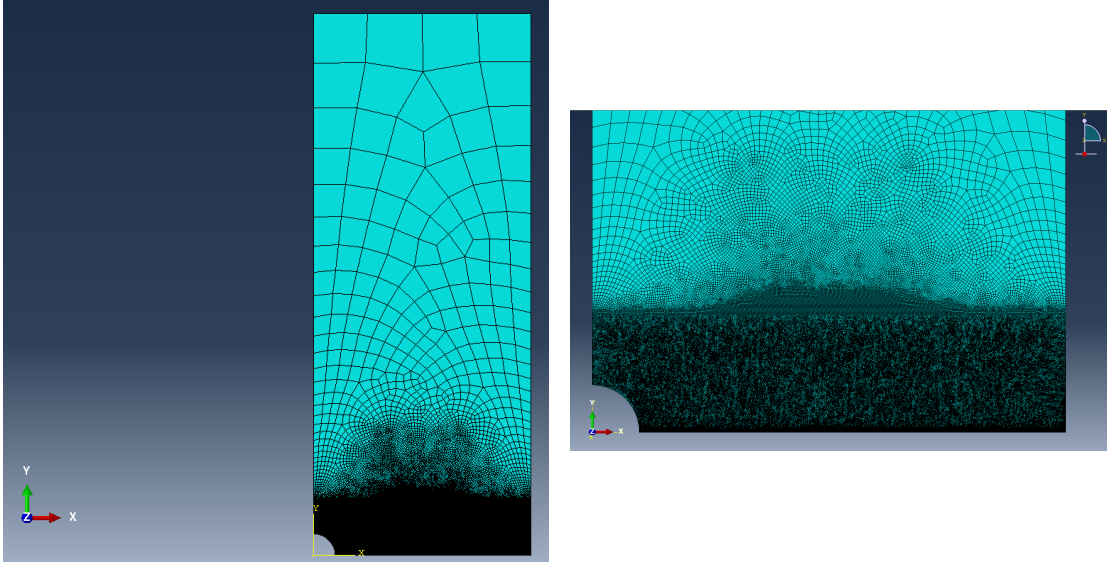


Figure 2.6: Mesh generated for a size effect analysis ($R = 2$ mm) and its detailed visualization. The element minimum size ($h_{\min} = \ell_2/5$) is fixed all along the bottom side. At a distance equal to 5 mm the element fixed size is $h_{\text{part}} = \ell_2$.

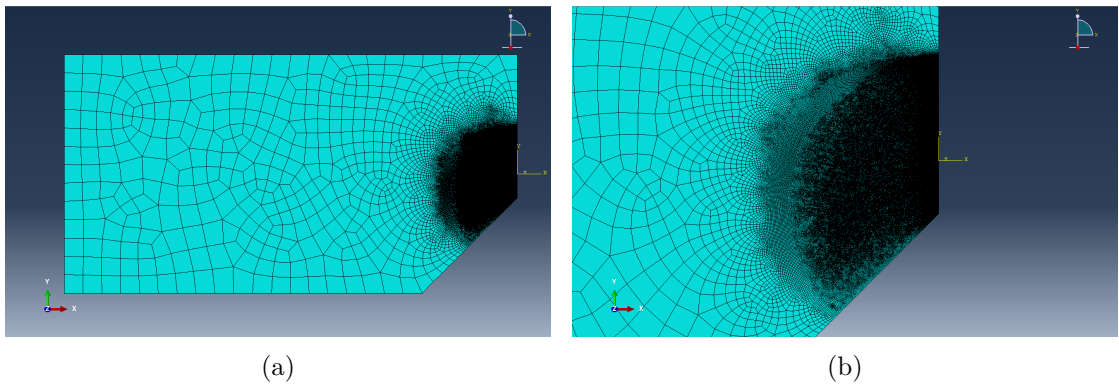


Figure 2.7: Mesh generated for a TPB analysis ($a = 2$ mm, $\beta = 90^\circ$) and its detailed visualization. The element minimum size ($h_{\min} = \ell_2/5$) is fixed along the right contour lower half: this refined zone does not reach the geometry top side for a significant critical load underestimation. All over the circumference arc (visible also in 2.5) the element fixed size is $h_{\text{part}} = \ell_2$.

2.4 FORTRAN subroutine structure

In this section the implemented FORTRAN code main features are discussed and analyzed, in order to fully comprehend subroutines logic and to interpret simulations output with the best premises. The code is recalled by Abaqus for every element involved in the analysis.

Here the UEL subroutine by [Martínez-Pañeda et al. \(2018\)](#) *incipit* is reported:

Listing 2.1: Phase-Field UEL subroutine *incipit*

```

1 module kvisual
2 implicit none
3 real*8 UserVar(500000,9,4)
4 integer nelem
5 save
6 end module
7
8 subroutine uel(rhs,amatrix,svars,energy,ndofel,nrhs,nvars,
9 1 props,nprops,coords,mcrd,nnode,u,du,v,a,jtype,time,dtime,
10 2 kstep,kinc,jelem,params,ndload,jdltyp,adlmag,predef,npredf,
11 3 lflags,mlvarx,ddlmg,mdload,pnewdt,jprops,njpro,period)
12
13 use kvisual
14 include 'aba_param.inc' !implicit real(a-h o-z)
15
16 dimension rhs(mlvarx,*),amatrix(ndofel,ndofel),props(*),svars(*),
17 1 energy(*),coords(mcrd,nnode),u(ndofel),du(mlvarx,*),v(ndofel),
18 2 a(ndofel),time(2),params(*),jdltyp(mdload,*),adlmag(mdload,*),
19 3 ddlmg(mdload,*),predef(2,npredf,nnode),lflags(*),jprops(*)
20
21 parameter(ndim=2,ntens=4,ninpt=4,nsvint=10)
22
23 dimension wght(ninpt),dN(nnode,1),dNdz(ndim,nnode),stran(ntens),
24 2 dNdx(ndim,nnode),b(ntens,nnode*ndim),ddsde(ntens,ntens),
25 3 stress(ntens),dstran(ntens),statevLocal(nsvint)

```

Among various initialization strings, in line 3 the variable $N_{\max} = 500000$ is set, referring to the maximum number of definable elements. From line 8 all the defined code variables and the extracted data from Abaqus are reported. The main ones are:

rhs: the array containing the contributions of the current element to the global residuals expression (i.e. \mathbf{r}_t^u and \mathbf{r}_t^α). Its dimensions are 12×1 , because the code works with quadrangular element and for every node we have 3 degree of freedom (u_x , u_y and α). The order is: $u_x^1, u_y^1, u_x^2, u_y^2, u_x^3, u_y^3, u_x^4, u_y^4, \alpha^1, \alpha^2, \alpha^3, \alpha^4$.

u: the vector enclosing all the unknowns in the abovementioned order.

amatrx: the matrix containing the contributions of the current element to the global stiffness matrix \mathbf{K} expression. Its dimensions are 12 X 12: recalling the structure displayed in (2.30) we have that \mathbf{K}^{uu} dimensions are 8 X 8, whereas $\mathbf{K}^{\alpha\alpha}$ dimensions are 4 X 4. Adopting the staggered approach:

$$\mathbf{amatrx} = \left[\begin{array}{c|c} \mathbf{K}^{uu} & 0 \\ \hline 0 & \mathbf{K}^{\alpha\alpha} \end{array} \right] \quad (2.38)$$

Then in the code, after some initialization steps, appears a `do` construct cycling over the element nodes (in fact, the variable `ninpt` refers to the current node and `ninpt = 4`, as shown in Listing 2.1, line 21):

Listing 2.2: `do` cycle over current element nodes - Ist part

```

1 do kintk=1,ninpt
2
3     call kshapefcn(kintk,ninpt,nnode,ndim,dN,dNdz)
4     call kjacobian(jelem,ndim,nnode,coords,dNdz,djac,dNdx,mcrd)
5
6     dvol=wght(kintk)*djac
7
8     b=0.d0
9     do inod=1,nnode
10         b(1,2*inod-1)=dNdx(1,inod)
11         b(2,2*inod)=dNdx(2,inod)
12         b(4,2*inod-1)=dNdx(2,inod)
13         b(4,2*inod)=dNdx(1,inod)
14     end do
15
16     alpha=0.d0
17     do inod=1,nnode
18         alpha=alpha+dN(inod,1)*u(ndim*nnode+inod)
19     end do
20
21     if (alpha.gt.1.d0) alpha=1.d0
22     .
23     .
24     .

```

In lines 3-4 the main code recalls two subfunctions (`kshapefcn` and `kjacobian`) in order to define the lagrangian basic functions (as reported in (2.27)) and their *global* derivatives, contained in the `dNdx` array. This matrix is then employed to calculate the Jacobian determinant (`djac`) in `kjacobian`. In line 6 the subroutine uses `djac` and some previously defined quadrature weights to evaluate the element surface `dvol`.

From line 8 to line 14 the \mathbf{B}^u matrix (\mathbf{b}) is built for the current element:

$$\mathbf{B}^u = [\mathbf{B}_1^u \mid \mathbf{B}_2^u \mid \mathbf{B}_3^u \mid \mathbf{B}_4^u] = \begin{bmatrix} \phi_{1,x} & 0 & \phi_{2,x} & 0 & \phi_{3,x} & 0 & \phi_{4,x} & 0 \\ 0 & \phi_{1,y} & 0 & \phi_{2,y} & 0 & \phi_{3,y} & 0 & \phi_{4,y} \\ \phi_{1,y} & \phi_{1,x} & \phi_{2,y} & \phi_{2,x} & \phi_{3,y} & \phi_{3,x} & \phi_{4,y} & \phi_{4,x} \end{bmatrix} \quad (2.39)$$

In 16-21 section the code calculates α over the whole considered element using the computational version of (2.26b). To avoid nonphysical exceedings ($\alpha > 0$) a check on line 21 is imposed.

Listing 2.3: do cycle over current element nodes - Π^{nd} part

```

1      .
2      .
3      .
4      dstran=matmul(b,du(1:ndim*nnode,1))
5
6      call kstatevar(kintk,nsvint,svars,statevLocal,1)
7
8      stress=statevLocal(1:ntens)
9      stran(1:ntens)=statevLocal((ntens+1):(2*ntens))
10     alphan=statevLocal(2*ntens+1)
11     Hn=statevLocal(2*ntens+2)
12
13     if (dtime.eq.0.d0) alphan=alpha
14
15     Psi=0.d0
16     do k1=1,ntens
17         Psi=Psi+stress(k1)*stran(k1)*0.5d0
18     end do
19
20     call kumat(props,ddsde,stress,dstran,ntens,statevLocal)
21     stran=stran+dstran
22
23     if (Psi.gt.Hn) then
24         H=Psi
25     else
26         H=Hn
27     endif
28
29     statevLocal(1:ntens)=stress(1:ntens)
30     statevLocal((ntens+1):(2*ntens))=stran(1:ntens)
31     statevLocal(2*ntens+1)=alpha
32     statevLocal(2*ntens+2)=H
33
34     call kstatevar(kintk,nsvint,svars,statevLocal,0)

```

In line 4 the numerical strain increment `dstran` is evaluated, referring to the discrete equation:

$$\delta \boldsymbol{\varepsilon}_h = \mathbf{B}^u \mathbf{u} \quad (2.40)$$

From line 6 to line 13 the last step variables are recovered through the vector `statevLocal`, to compute subsequently H as defined in (2.24). The 15-18 section represents the code part where the elastic energy density $\psi_0 = \psi_0(\boldsymbol{\varepsilon})$ is calculated, recollecting that:

$$\psi_0(\boldsymbol{\varepsilon}) = \frac{1}{2} \boldsymbol{\varepsilon}^T \mathbb{A}_0 \boldsymbol{\varepsilon} = \frac{1}{2} \boldsymbol{\sigma}_0 \boldsymbol{\varepsilon} \quad (2.41)$$

In lines 20-21 an `UMAT` type subfunction (User-defined `MATerial`) is recalled: it delineates the material mechanical behavior through the definition of `ddsdde` and `stress` (i.e. the \mathbb{A}_0 and $\boldsymbol{\sigma}_0$ tensors computational versions).

In section 23-27 the damage irreversibility condition (2.24) is implemented, noting that `Psi` is the elastic energy evaluated for the current time \mathbf{t}^* and `Hn` (H_t equivalent) is the maximum energy value computed until $\mathbf{t}^* - dt$. In section 29-34 the history variables vector `statevLocal` is updated for the next subroutine recall.

Listing 2.4 reports the residuals and global stiffness matrix components contributions regarding the `kintk`-th node of the considered element. In Table 2.2 correspondences between Listing 2.4 code lines with residuals and stiffness matrix expressions are shown.

Listing 2.4: do cycle over current element nodes - IIIrd part

```

1      .
2      .
3      .
4      amatrix(1:8,1:8)=amatrix(1:8,1:8)+
5      1 dvol*((1.d0-alphan)**2+xk)
6      2 *matmul(matmul(transpose(b),ddsdde),b))
7
8      rhs(1:8,1)=rhs(1:8,1)-
9      1 dvol*(matmul(transpose(b),stress)*((1.d0-alphan)**2+xk))
10
11     amatrix(9:12,9:12)=amatrix(9:12,9:12)
12     1 +dvol*(matmul(transpose(dNdx),dNdx)*Gc*xlc
13     2 +matmul(dN,transpose(dN))*(Gc/xlc+2.d0*H))
14
15     rhs(9:12,1)=rhs(9:12,1)
16     1 -dvol*(matmul(transpose(dNdx),matmul(dNdx,u(9:12)))
17     2 *Gc*xlc+dN(:,1)*((Gc/xlc+2.d0*H)*alpha-2.d0*H))
18
19
20     UserVar(jelem,1:4,kintk)=statevLocal(1:ntens)*((1.d0-alphan)**2+k)
21     UserVar(jelem,5:9,kintk)=statevLocal((ntens+1):(2*ntens+1))
22
23 end do

```

Lines 4-6	(2.30b)	$K_{ij}^{uu} = \frac{\partial \mathbf{r}_i^u}{\partial \mathbf{u}_j} = \int_{\Omega} \left\{ g(\alpha_t) (\mathbf{B}_i^u)^T \mathbb{A}_0 \mathbf{B}_j^u \right\} d\Omega$
Lines 8-9	(2.29a)	$\mathbf{r}_j^u = \int_{\Omega} \left\{ g(\alpha_t) (\mathbf{B}_j^u)^T \boldsymbol{\sigma}_0 - (\boldsymbol{\Phi}_j)^T \mathbf{f} \right\} d\Omega$
Lines 11-13	(2.30d)	$K_{ij}^{\alpha\alpha} = \frac{\partial r_i^{\alpha}}{\partial \alpha_j} = \int_{\Omega} \left\{ \left(2H + \frac{G_c}{\ell} \right) \phi_i \phi_j + (\mathbf{B}_i^{\alpha})^T G_{cl} \mathbf{B}_j^{\alpha} \right\} d\Omega$
Lines 15-17	(2.29b)	$r_j^{\alpha} = \int_{\Omega} \left\{ -2(1 - \alpha) \phi_j H + G_c \left[\frac{\alpha}{\ell} \phi_j + \ell (\mathbf{B}_j^{\alpha})^T \nabla \alpha \right] \right\} d\Omega$

Table 2.2: Correspondences between Listing 2.4 code lines with residuals and stiffness matrix expressions.

Chapter 3

2D simulations results

With a view to validate and leverage phase-field models in brittle fracture mechanics framework to predict structural failure stresses, two-dimensional simulations outcomes will be presented, discussed and compared with their correspondent reference experimental results.

It is worth recalling that two different case studies were chosen: the first one concerning the hole size influence on the failure stress in slabs, whereas the second focuses the re-entrant corners role in structural resistance decrease: the latter analysis were performed through Three Point Bending tests, so we will refer to this case study with **TPB tests**.

3.1 Circular Holes: size effect

The aim of this case study is to replicate *in sicilio* [Kirsch \(1898\)](#) analytical solution regarding the stress concentration factor K_+ on a holed infinite plate under uni-axial loading, as shown in [Fig. 3.1](#) and [Eq. \(3.1\)](#).

$$K_+ = \frac{\sigma_{\vartheta, \max}}{\sigma} = 3$$

$$K_+ = \text{stress concentration factor} \tag{3.1}$$

$$\sigma_{\vartheta, \max} = \text{maximum circumferential stress}$$

$$\sigma = \text{nominal stress}$$

Given the problem setup ideality (i.e. the *infinite* plate⁶) the aim of this work is to verify that, by increasing hole radius R , the critical failure stress decreases from σ_M ($R = 0$) to $\sigma_M/3$ (sufficiently large R , but still small with respect the plate size), where σ_M represents the ultimate tensile strength.

To conduct this specific analysis [Sapora et al. \(2018\)](#) is employed as reference paper regarding experimental results and geometry definitions (as shown in [Subsect. 2.3.1](#)) and

⁶Following [Li and Zhang \(2006\)](#) recommendations ($w/2R > 10$) the infinite plate hypothesis is acceptable for all the considered geometry setups.

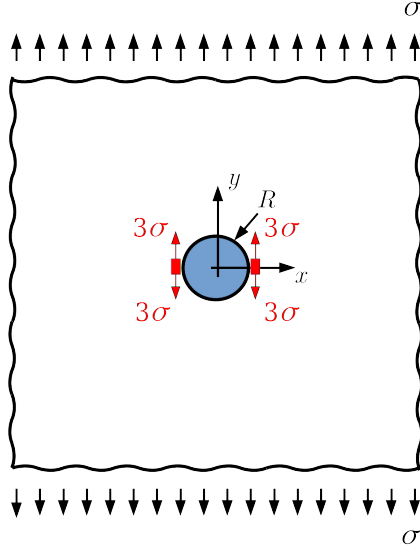


Figure 3.1: Infinite tensile plate containing a circular hole. Maximum circumferential stress $\sigma_{\theta, \max} = 3\sigma$ is highlighted.

Ayatollahi and Torabi (2010) and Torabi et al. (2016) for material properties. The available experimental results refer to uni-axial tensile load tests involving two brittle material species (polymethylmethacrylate, or PMMA, and general purpose polystyrene, or GPPS) that constitute slab structures incorporating circular holes of four different measures ($R = 0.25, 0.5, 1, 2$ mm).

3.1.1 Materials properties definition

In the following the material properties necessary for numerical simulations will be evaluated. From Ayatollahi and Torabi (2010), regarding PMMA:

$$\begin{aligned} E &= 2960 \text{ MPa}, & \nu &= 0.38, \\ \sigma_M &= 70.5 \text{ MPa}, & K_{\text{IC}} &= 1.96 \text{ MPa}\sqrt{\text{m}} = 61.98 \text{ MPa}\sqrt{\text{mm}} \end{aligned} \quad (3.2)$$

As input values we need also the numerical characteristic length ℓ and the critical energy release rate G_c . Recollecting Irwin's relations (2.18) and (2.34):

$$G_c = \frac{K_{\text{IC}}^2}{E'} = \frac{K_{\text{IC}}^2 (1 - \nu^2)}{E} = 1.11 \text{ MPa} \cdot \text{mm} \quad (3.3a)$$

$$\sigma_M = \sqrt{\frac{G_c E}{\ell_{\text{ch}}}} \rightarrow \ell_{\text{ch}} = \frac{G_c E}{\sigma_M^2 (1 - \nu^2)} = 0.773 \text{ mm} \quad (3.3b)$$

An AT2 phase-field model type is implemented, so recalling (2.19b):

$$\ell = \ell_2 = \frac{27}{256} \ell_{\text{ch}} = 81.53 \cdot 10^{-3} \text{ mm} \quad (3.4)$$

Another important simulation variable is the mesh minimum size h_{min} (see Subsect. 2.3.4):

$$h_{\text{min}} = \frac{\ell_2}{5} = 16.3 \cdot 10^{-3} \text{ mm} \quad (3.5)$$

The same procedure has been followed for GPPS properties. Collecting the following values from Torabi et al. (2016):

$$\begin{aligned} & \begin{cases} E & = 3100 \text{ MPa} \\ \nu & = 0.34 \\ \sigma_M & = 30 \text{ MPa} \\ K_{\text{IC}} & = 44.27 \text{ MPa}\sqrt{\text{mm}} \end{cases} \\ \Rightarrow & \begin{cases} G_c & = \frac{K_{\text{IC}}^2}{E'} = 0.56 \text{ MPa} \cdot \text{mm} \\ \ell_{\text{ch}} & = \frac{G_c E}{\sigma_M^2 (1-\nu^2)} = 2.18 \text{ mm} \\ \ell & = \ell_2 = \frac{27}{256} \ell_{\text{ch}} = 0.229 \text{ mm} \\ h_{\text{min}} & = \frac{\ell_2}{5} = 45.94 \cdot 10^{-3} \text{ mm} \end{cases} \end{aligned} \quad (3.6)$$

The evaluated properties for both materials are summarized in Tables 3.1 and 3.2.

	E [MPa]	ν	σ_M [MPa]	K_{IC} [MPa $\sqrt{\text{mm}}$]
PMMA	2960	0.38	70.5	61.98
GPPS	3100	0.34	30	44.27

Table 3.1: Measured experimental material properties: Young’s modulus E , Poisson’s ratio ν , ultimate tensile strength σ_M and fracture toughness K_{IC} . For PMMA properties are taken from Ayatollahi and Torabi (2010), whereas for GPPS from Torabi et al. (2016).

	G_c [MPa \cdot mm]	ℓ_{ch} [mm]	ℓ_2 [mm]	h_{min} [mm]
PMMA	1.11	0.773	$81.53 \cdot 10^{-3}$	$16.3 \cdot 10^{-3}$
GPPS	0.56	2.18	0.229	$45.94 \cdot 10^{-3}$

Table 3.2: Derived material properties: critical energy release rate G_c , physical characteristic length ℓ_{ch} , numerical characteristic length ℓ_2 and minimum mesh element size h_{min} .

3.1.2 PMMA results

Reference experimental results and numerical outcomes are reported in Table 3.3. It should be noted that the original data refer to *load* measures. In fact, our reported stress

values are calculated as:

$$\sigma_{cr} = \frac{P_{cr}}{lt} = \frac{P_{cr}}{400 \text{ mm}^2},$$

where l and t are specimen length and thickness respectively, as listed in Table 2.1. Conducted numerical simulations yields a σ_{cr} slight overestimation for every considered hole radius measure.

Graphical confrontation between the two datasets is displayed in Fig. 3.2. Another important analysis feature is that the critical values are normalized with respect to their respective failure nominal stresses $\sigma(0) = \sigma_0$. For the experimental data basis, $\sigma_0 = \sigma_M$. Numerical outcomes (marked with green dots) are clearly in good agreement with the experimental average values.

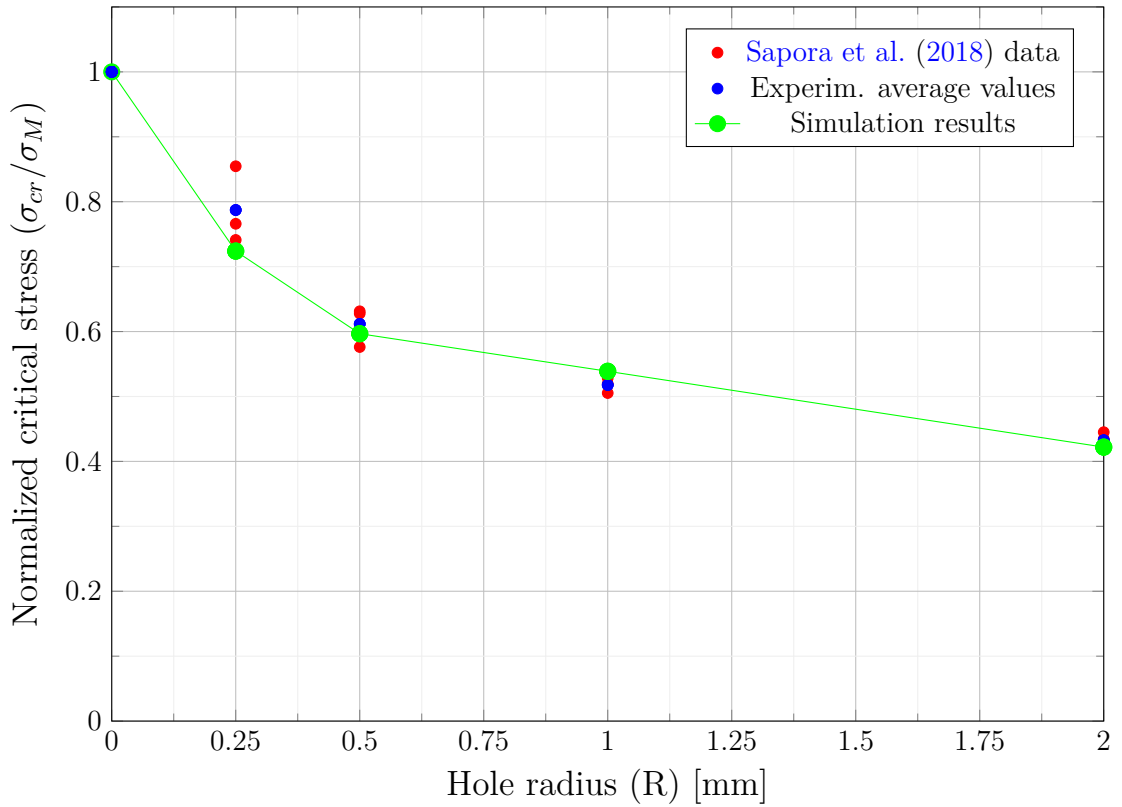


Figure 3.2: PMMA failure stress σ_{cr} experimental results and the respective numerical outcomes depending on hole radius R . The graphical comparison reveals a good matching between the two datasets.

σ_{cr} [MPa] \backslash R [mm]	0	0.25	0.5	1	2
Sapora et al. (2018) (avg.)	$\sigma_M = 70.5$	55.5	43.125	36.5	30.5
Simulation results	78.854	57.085	47.053	44.049	33.28

Table 3.3: PMMA failure stress σ_{cr} experimental results and respective numerical outcomes. Simulations mildly overestimate real failure stress values for all the considered radii.

3.1.3 GPPS results

Average experimental results from Sapora et al. (2018) and numerical outputs are reported in Table 3.4. Differently from the PMMA case, computational stresses slightly overestimate the real ones for $R = 0.5, 1, 2$ mm. The comparison between experimental and numerical normalized critical stress shown in Fig. 3.3 reveals a good agreement between the two datasets. The only exception is for $R = 0.25$ mm, where the numerical outcome underestimates the real structure resistance (this feature is observable in a less marked way also for PMMA case study). The structural resistance decrease for GPPS is slower than the PMMA case: in fact, the structure critical stress is only halved for $R = 2$ mm. This apparent mismatch (recalling that the expected stress concentration factor $K_+ = 3$) depends on the independent variable choice for the post-processing plotting step (i.e. radius hole R): in fact, normalizing also the radius hole with respect to the characteristic length ℓ_{ch} and plotting on the same graph both PMMA and GPPS datasets (Figure 3.4) our numerical results lie on a single 'Phase-Field curve' that tends to the expected resistance decrease value. In Fig. 3.4 are also reported the experimental reference values from Sapora et al. (2018), reposing the comparison already shown in Fig. 3.2 and 3.3, and the Finite Fracture Mechanics theoretical trend from Sapora and Cornetti (2018). Despite their different slopes, the numerical and theoretical decrease predictions tends both to the expected value (i.e. σ_{cr} decreases from σ_M ($R = 0$) to $\sigma_M/3$ for sufficiently large R , but still small with respect to the plate size).

σ_{cr} [MPa] \backslash R [mm]	0	0.25	0.5	1	2
Sapora et al. (2018) (avg.)	$\sigma_M = 30$	27.281	21.719	18.125	15.781
Simulation results	26.872	20.776	18.478	16.671	15.004

Table 3.4: GPPS failure stress σ_{cr} experimental results and respective numerical outcomes. Simulations mildly overestimate real failure stress values for $R = 0.5, 1, 2$ mm. Critical stress estimations underestimate experimental data for $R = 0$ mm (no hole case, σ_M prediction) and $R = 0.25$ mm.

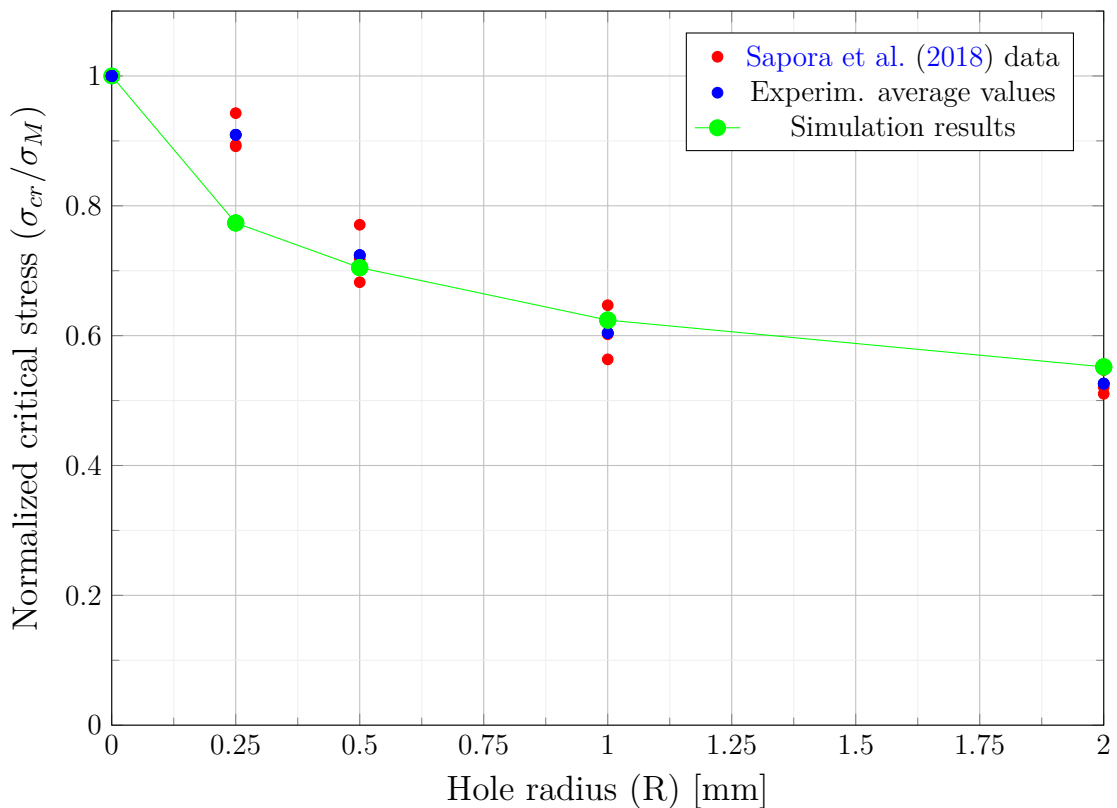


Figure 3.3: GPPS failure stress σ_{cr} experimental results and the respective numerical outcomes depending on hole radius R .

3.2 Strength decrease due to sharp V-notches

It is well known that sharp V-notches have a significant impact on structural resistance, inducing a severe material nominal failure stresses decrease. From the pioneering paper by [Williams \(1952\)](#) that provided first crucial analytical results, several research works (as [Carpinteri \(1987\)](#)) have focused on the influence of the notch amplitude on the structural strength. The purpose of this section is to show and examine numerical outcomes, implementing the discussed phase-field fracture model for this case study.

[Carpinteri \(1987\)](#) is the experimental reference paper: in this study the only involved material is PMMA, whose properties are reported in Tables 3.1 and 3.2. The ultimate tensile strength $\sigma_M = 70.5$ MPa is the same implemented for the analysis about the size effect of circular holes. This choice was forced by simulation computational costs, in fact:

$$\ell_{ch} \propto \sigma_M^{-2}, \quad (3.7)$$

suggesting that for higher σ_M the characteristic length ℓ_{ch} decreases quadratically. This brings to a computational cost increase that our facilities could not afford for $\sigma_M > 80$ MPa. Two different notch depths, namely $a = 1$ cm and $a = 2$ cm, were considered.

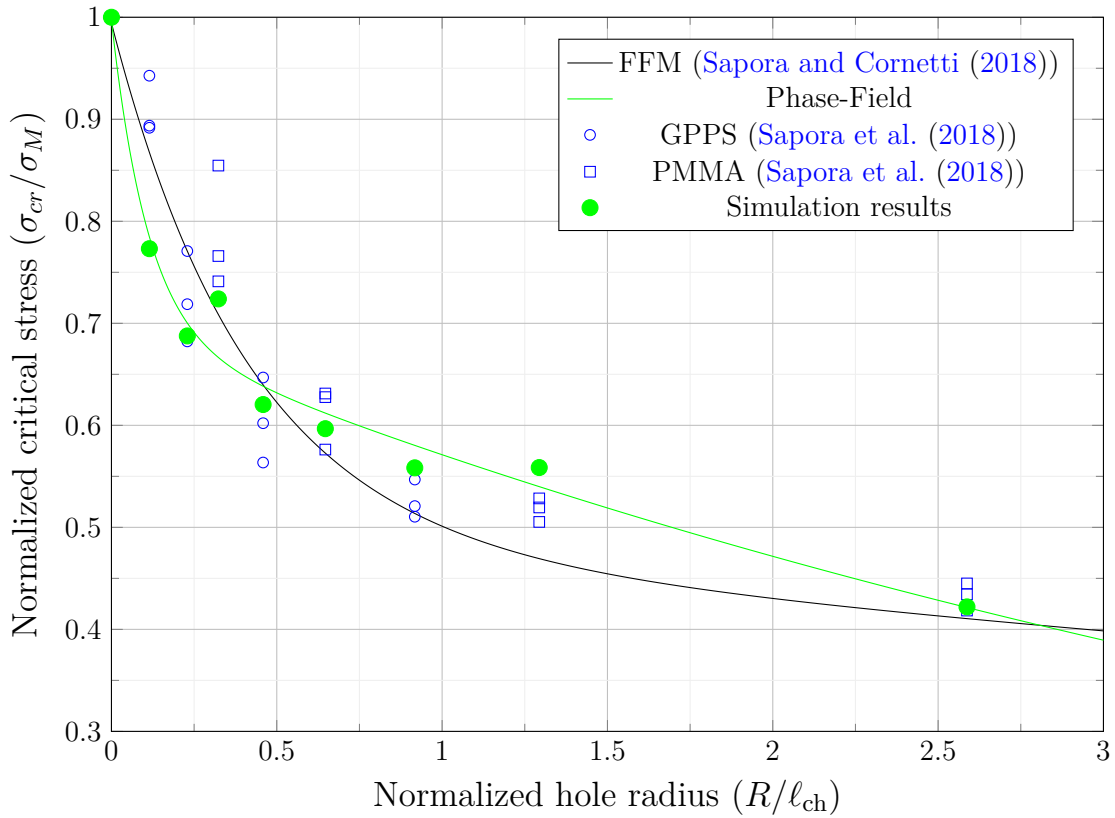


Figure 3.4: Normalized failure stress σ_{cr} numerical results (both PMMA and GPPS datasets), corresponding experimental values (from Sapora et al. (2018)) and the resistance decrease trend predicted by Finite Fracture Mechanics (from Sapora and Cornetti (2018)). Despite their different slopes, the numerical and theoretical decrease predictions tends both to the expected value (i.e. σ_{cr} decreases from σ_M ($R = 0$) to $\sigma_M/3$ for sufficiently large R , but still small with respect to the plate size).

3.2.1 $a = 1$ cm

Table 3.5 contains experimental and numerical critical load values P_{cr} . It is clear that simulations failed to predict real P_{cr} results for the unnotched case ($\beta = 180^\circ$) and generally Abaqus outcomes do not match the respective experimental data. Fig. 3.5 shows *normalized* critical load datasets with respect to P_{180° (i.e. $P_{cr}(\beta = 180^\circ)$): by adopting this alternative graphical choice, numerical decrease trend fully captures the experimental outcomes. Table 3.6 gathers the adimensional load measures for both frameworks. One of the auspicious research development is to conduct simulations on more powerful computers to verify also a quantitative good prediction about resistance decrease.

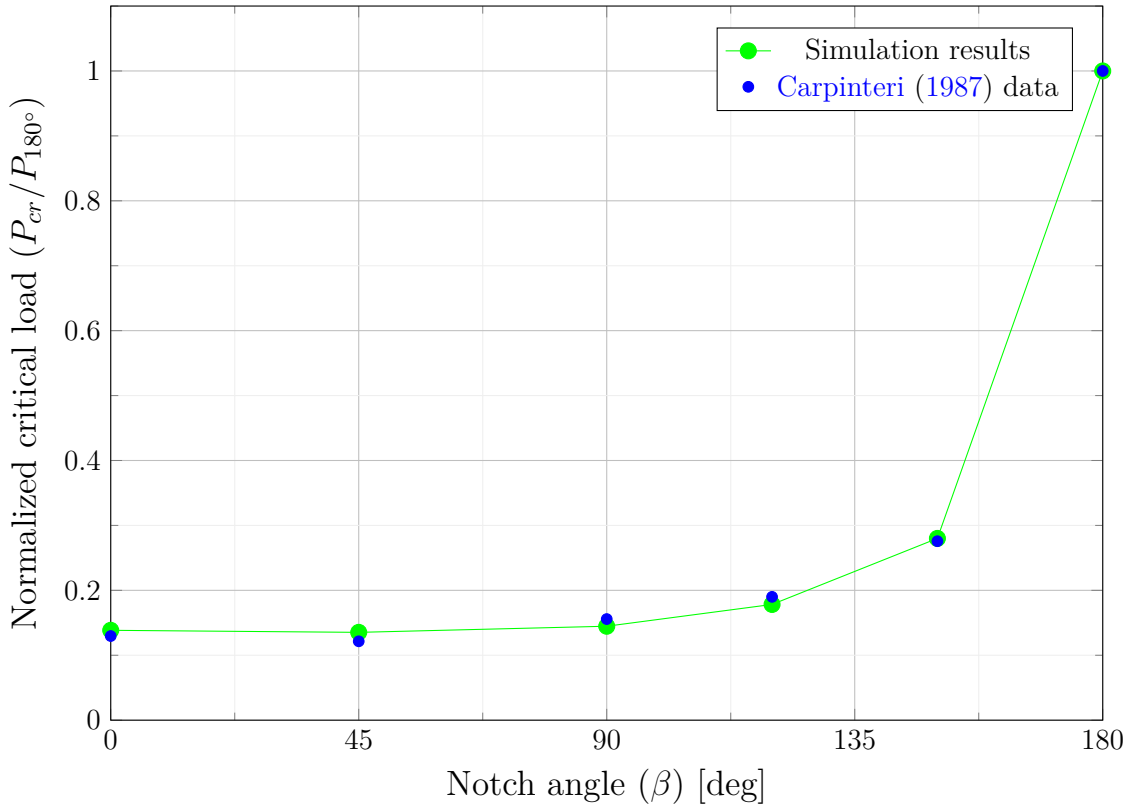


Figure 3.5: Failure load P_{cr} numerical and experimental results depending on notch angle β for $\mathbf{a} = \mathbf{1\ cm}$. Datasets are normalized with respect to the unnotched case critical value (i.e. $P_{180^\circ} = P_{cr}(\beta = 180^\circ)$). The graphical comparison reveals a quite perfect matching between the two datasets.

P_{cr} [N] \ β [deg]	180	150	120	90	45	0
Carpinteri (1987) (avg.)	$P_M = 3827$	1055	727	596	465	496
Simulation results	2383.9	667.5	425	345	322.5	330

Table 3.5: Failure load P_{cr} experimental results and respective numerical outcomes for $\mathbf{a} = \mathbf{1\ cm}$. Simulation data do not match the respective experimental values.

3.2.2 $\mathbf{a} = \mathbf{2\ cm}$

Table 3.7 includes physical testing and computational critical loads P_{cr} for a notch depth $a = 2\ \text{cm}$. Even in this case simulation results do not capture exactly the experimental trend, but a moderate degree of consistency is observed.

Fig. 3.6 illustrates the two *normalized* datasets with respect to P_{180° , revealing that the numerical predictions accord very closely with the experimental results. For the sake of good order, Table 3.8 contains the normalized experimental and numerical datasets.

P_{cr}/P_{180° \ β [deg]	180	150	120	90	45	0
Carpinteri (1987) (avg.)	1	0.27567	0.18997	0.15574	0.12151	0.12961
Norm. simulation results	1	0.27999	0.17828	0.14472	0.13528	0.13843

Table 3.6: Failure load P_{cr} experimental results and respective numerical outcomes for $\mathbf{a} = \mathbf{1}$ cm. Differently from Table 3.5, values are normalized with respect to $P_{180^\circ} = P_{cr}(\beta = 180^\circ)$. Normalized experimental and numerical datasets match correctly.

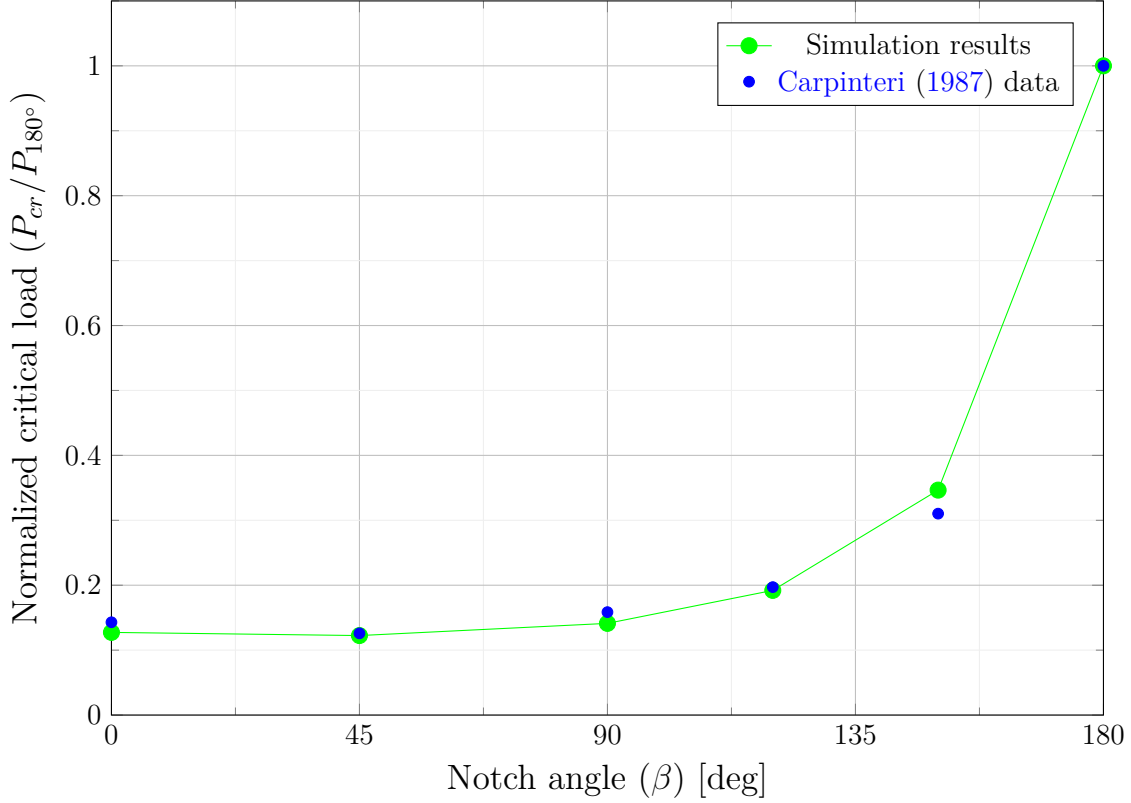


Figure 3.6: Failure load P_{cr} numerical and experimental results depending on notch angle β for $\mathbf{a} = \mathbf{2}$ cm. Datasets are normalized with respect to the unnotched case critical value (i.e. $P_{180^\circ} = P_{cr}(\beta = 180^\circ)$). The graphical comparison reveals a near-perfect alignment between the two datasets.

P_{cr} [N] \backslash β [deg]	180	150	120	90	45	0
Carpinteri (1987) (avg.)	$P_M = 2050$	636	404	325	258	293
Simulation results	1796.7	622.5	345	253.75	220	228.75

Table 3.7: Failure load P_{cr} experimental results and respective numerical outcomes for $\mathbf{a} = \mathbf{2\ cm}$. Although simulation data do not match the respective experimental values, a moderate level of agreement is observed.

P_{cr}/P_{180° \backslash β [deg]	180	150	120	90	45	0
Carpinteri (1987) (avg.)	1	0.31024	0.19707	0.15854	0.12585	0.14293
Simulation results	1	0.34648	0.19202	0.14123	0.12245	0.12732

Table 3.8: Failure load P_{cr} experimental results and respective numerical outcomes for $\mathbf{a} = \mathbf{2\ cm}$. Differently from Table 3.7, values are normalized with respect to $P_{180^\circ} = P_{cr}(\beta = 180^\circ)$. Normalized experimental and numerical datasets are in quite perfect alignment.

Chapter 4

Conclusions and future perspectives

Fracture mechanics has attracted research attention since the birth of modern building sciences. As new artificial materials, such as composites, are introduced in construction disciplines, research into fracture mechanics has been renewed.

In this dissertation, Phase-Field models were theoretically defined and put at the service of computational brittle fracture mechanics, proving to be a potentially reliable and robust numerical tool to predict the strength of structural components.

In Chapter 1 a deep analysis on phase-field models' bounds with Griffith (1921) fracture theory and variational methods was conducted, starting from the introduction of the energy functional by Tanné et al. (2017). An original MATLAB® code resolving a one-dimensional fracture problem was broadly examined, based on the experimental and numerical setup by Pham et al. (2011): related results describe successfully the damaging phase instability, which depends on bar dominant length L of the bar.

Phase-Field model applications were then extended to two-dimensional domains, allowing for a wider range of case studies to be explored. In Chapter 2, model theoretical features were deepened to enhance the implementation, following the studies carried out by Martínez-Pañeda et al. (2018) and Navidtehrani et al. (2021) who developed the numerical framework by coupling Abaqus and FORTRAN subroutines.

Chapter 3 gathered two-dimensional numerical outcomes regarding two fracture mechanics case studies: a circular hole in an infinite tensile plate, and a sharp V-notched structure under Three Point Bending (TPB). As regards the former geometry, numerical results were compared with experimental one presented in Sapora et al. (2018) concerning PMMA and GPPS. For both materials, the agreement was generally more than satisfactory. More specifically, numerical simulations were able to catch the transition from σ_M ($R = 0$) to $\sigma_M/3$ for sufficiently large R , but still small with respect to the plate size. As regards the latter geometry, model outcomes were applied to analyse the influence of re-entrant corners on the brittle failure behaviour. Numerical (normalized) failure loads were successfully compared with experimental data on PMMA by Carpinteri (1987), although the huge computational effort.

This dissertation opens up to several future improvements. To cite but a few:

- The optimization of the adopted mesh, to minimize the computational effort.
- The generalization of the model to investigate crack propagation after initiation.
- Phase-Field model implementation on FEniCS, a computing platform for partial differential equation resolution.

Bibliography

- T. Q. Ansari, H. Huang, and S. Q. Shi. Phase field modeling for the morphological and microstructural evolution of metallic materials under environmental attack. *npj Computational Materials*, 2021.
- M.R. Ayatollahi and A.R. Torabi. Investigation of mixed mode brittle fracture in rounded-tip v-notched components. *Engineering Fracture Mechanics*, 2010.
- A. Benallal and J.J. Marigo. Bifurcation and stability issues in gradient theories with softening. *Modelling and Simulation in Materials Science and Engineering*, 2006.
- A. Braides. *Gamma-convergence for beginners*. Oxford University Press, 2002.
- A. Carpinteri. Stress-singularity and generalized fracture toughness at the vertex of re-entrant corners. *Engineering Fracture Mechanics*, 1987.
- A. Carpinteri. *Scienza delle costruzioni 2*. Pitagora Editrice, Bologna, 1992.
- C. Comi and U. Perego. Fracture energy based bi-dissipative damage model for concrete. *International Journal of Solids and Structures*, 2001.
- G. Francfort and J.J. Marigo. Revisiting brittle fracture as an energy minimization problem. *Journal of The Mechanics and Physics of Solids - J MECH PHYS SOLIDS*, 1998.
- S. I. Gass and M. C. Fu. *Karush-Kuhn-Tucker (KKT) Conditions*. Springer US, 2013.
- A.A. Griffith. The phenomena of rupture and flow in solids. *Philosophical Transactions of the Royal Society of London Series*, 1921.
- C.E. Inglis. Stresses in a plate due to the presence of cracks and sharp corners. *Proc. Inst. Naval. Arch.*, 1913.
- G.R. Irwin. Analysis of stresses and strains near the end of a crack traversing a plate. *Journal of Applied Mechanics*, 1957.
- E.G. Kirsch. Die theorie der elastizitat und die bedurfnisse der festigkeitslehre. *Zantralblatt Verlin Deutscher Ingenieure*, 1898.
- G. Lancioni and G. Royer-Carfagni. The variational approach to fracture mechanics. a practical application to the french panthéon in paris. *Journal of Elasticity*, 2009.

- J. Li and X.B. Zhang. A criterion study for non-singular stress concentrations in brittle or quasi-brittle materials. *Engineering Fracture Mechanics*, 2006.
- Z. Li, Z. Qiao, and T. Tang. *Finite Element Methods for 1D Boundary Value Problems*. Cambridge University Press, 2017.
- J.J. Marigo and K. Pham. Stability of non localized responses for damaging materials. *Vietnam Journal of Mechanics*, 2009.
- E. Martínez-Pañeda, A. Golahmar, and C. F. Niordson. A phase field formulation for hydrogen assisted cracking. *Computer methods in applied mechanics and engineering*, 2018.
- C. Miehe, F. Welschinger, and M. Hofacker. Thermodynamically consistent phase-field models of fracture: Variational principles and multi-field finite elements implementations. *International Journal for Numerical Methods in Engineering*, 2010.
- Y. Navidtehrani, C. Betegón, and E. Martínez-Pañeda. A unified abaqus implementation of the phase field fracture method using only a user material subroutine. *Materials*, 2021.
- K. Pham, H. Amor, J.J. Marigo, and C. Maurini. Gradient damage models and their use to approximate brittle fracture. *International Journal of Damage Mechanics*, 2011.
- A. Sapora and P. Cornetti. Crack onset and propagation stability from a circular hole under biaxial loading. *International Journal of Fracture*, 2018.
- A. Sapora, A.R. Torabi, S. Etesam, and P. Cornetti. Finite fracture mechanics crack initiation from a circular hole. *Fatigue and Fracture of Engineering Materials and Structures*, 2018.
- Z. Shuwei, Z. Xiaoying, and R. Timon. Phase-field modeling of fluid-driven dynamic cracking in porous media. *Computer Methods in Applied Mechanics and Engineering*, 2019.
- M. Smith. *ABAQUS Analysis User's Manual, Version 6.9*. Dassault Systèmes Simulia Corp, 2009.
- G. Stewart. *Polynomial Interpolation*. Society for Industrial and Applied Mathematics, 1996.
- E. Tanné, L. Tianyi, B. Bourdin, J.J. Marigo, and C. Maurini. Crack nucleation in variational phase-field models of brittle fracture. *Journal of the Mechanics and Physics of Solids*, 2017.
- D. Taylor. *The Theory of Critical Distances - A New Perspective in Fracture Mechanics*. Elsevier, Oxford, UK, 2007.
- A.R. Torabi, H.R. Majidi, and M.R. Ayatollahi. Brittle failure of key-hole notches under mixed mode i/ii loading with negative mode i contributions. *Engineering Fracture Mechanics*, 2016.

BIBLIOGRAPHY

H.M.W. Westergaard. Bearing pressures and cracks. *Journal of Applied Mechanics*, 1939.

M. L. Williams. Stress singularities resulting from various boundary conditions in angular corners of plates in extension. *Journal of Applied Mechanics*, 1952.